energies

MDPI

Article

Fuel Cell–Battery Hybrid Trains for Non-Electrified Lines: A Dynamic Simulation Approach

Giuliano Agati [1], Domenico Borello [1,*], Alessandro Ruvio [2] and Paolo Venturini [1]

[1] Department of Mechanical and Aerospace Engineering, Sapienza University of Rome, 00184 Rome, Italy; giuliano.agati@uniroma1.it (G.A.); paolo.venturini@uniroma1.it (P.V.)
[2] Department of Astronautical, Electrical and Energy Engineering, Sapienza University of Rome, 00184 Rome, Italy; alessandro.ruvio@uniroma1.it
* Correspondence: domenico.borello@uniroma1.it

Abstract

Hydrogen-powered hybrid trains equipped with fuel cells (FC) and batteries represent a promising alternative to diesel traction on non-electrified railway lines and have significant potential to support modal shifts toward more sustainable transport systems. This study presents the development of a flexible MATLAB-based tool for the dynamic simulation of fuel cell–battery hybrid powertrains. The model integrates train dynamics, rule-based energy management, system efficiencies, and component degradation, enabling both energy and cost analyses over the vehicle's lifetime. The objective is to assess the techno-economic performance of different powertrain configurations. Sensitivity analyses were carried out by varying two sizing parameters: the nominal power of the fuel cell (parameter m) and the total battery capacity (parameter n), across multiple real-world railway routes. Results show a slight reduction in lifecycle costs as m increases (5.1 €/km for m = 0.50) mainly due to a lower FC degradation. Conversely, increasing battery capacity (n) lowers costs by reducing cycling stress for both battery and FC, from 5.3 €/km (n = 0.10) to 4.5 €/km (n = 0.20). In general, lowest values of m and n provide unviable solutions as the battery discharges completely before the end of the journey. The study highlights the critical impact of the operational profile: for a fixed powertrain configuration (m = 0.45, n = 0.20), the specific cost dramatically increases from 4.44 €/km on a long, flat route to 15.8 €/km on a hilly line and up to 76.7 €/km on a mountainous route, primarily due to severe fuel cell degradation under transient loads. These findings demonstrate that an "all-purpose" train sizing approach is inadequate, confirming the necessity of route-specific powertrain optimization to balance techno-economic performance.

Keywords: decarbonization; sustainable mobility; railways; hydrogen trains; battery–fuel cell powertrain; hydrogen hybrid systems; energy management system; sizing sensitivity analysis

check for updates

Academic Editor: Felix Barreras

Received: 6 August 2025
Revised: 26 September 2025
Accepted: 2 October 2025
Published: 16 October 2025

Citation: Agati, G.; Borello, D.; Ruvio, A.; Venturini, P. Fuel Cell–Battery Hybrid Trains for Non-Electrified Lines: A Dynamic Simulation Approach. *Energies* **2025**, *18*, 5457. https://doi.org/10.3390/en18205457

Copyright: © 2025 by the authors. Licensee MDPI, Basel, Switzerland. This article is an open access article distributed under the terms and conditions of the Creative Commons Attribution (CC BY) license (https://creativecommons.org/licenses/by/4.0/).

1. Introduction

In the broader context of the global energy transition, it is imperative that all sectors accelerate the adoption of renewable energy sources and pursue decarbonization strategies. The railway sector plays a pivotal role in reducing emissions, as it constitutes a fundamental component of both passenger and freight transportation on a global scale. In the EU-27, 56.6% of the railway network is electrified, ranging from 2.8% in Ireland to 100% in Switzerland [1]. In Italy, approximately 29% of the 16,781 km of the National Railway Network

is still non-electrified. The electrification of these lines is identified as a key strategy to further reduce carbon emissions in the railway sector. However, it is noteworthy that non-electrified lines generally account for a relatively low percentage of total passenger traffic (i.e., 12% in Italy [2]). This suggests that the comprehensive electrification of these lines is economically unviable due to the substantial costs and technical challenges associated with the process. Consequently, the future of these lines may entail a significant reliance on diesel traction or even lead to their discontinuation, which would result in considerable inconvenience for passengers. Therefore, there is an imperative to explore alternative technological solutions capable of replacing diesel propulsion on such routes. Moreover, as in general railways have lower emissions impact with respect to other transportation segments, expanding its national coverage could have a significant potential for modal shifts towards more sustainable transport systems, contributing to decarbonization efforts across the sector [3].

In 2019, the Fuel Cells and Hydrogen Joint Undertaking published the Hydrogen Roadmap Europe, which set out a strategy for the development of hydrogen energy up to the years 2030 and 2050 [4]. The analysis carried out, in an ambitious scenario, estimates that the transportation sector could have the highest need for hydrogen. In the rail sector, it is expected that by 2030 electric trains powered by fuel cells could replace about 570 diesel trains. Hydrogen-powered trains might be used on non-electrified lines or on light rails, where fuel cell-powered trams could be used [5]. In 2020, the European Community has acknowledged the long-term potential of sustainable alternative fuels to replace fossil fuels [6], with hydrogen emerging as one of the most promising options [7]. The use of hydrogen-powered trains confers several advantages, including the elimination of carbon dioxide emissions, and a reduction in noise levels in particulate emissions.

The utilization of fuel cell hybrid (FCH) trains and other vehicles has been a subject of investigation in recent years. For instance, Fragiacomo et al. [8] proposes four powertrain configurations, based on suitable combinations of fuel cells and/or batteries, as a replacement or supplement for a diesel/overhead line powertrain on a real passenger train, which was tested on an existing regional track. The development of an energy management system for a FC hybrid tramway was the subject of investigation in [9]. Agati et al. [7] studied the effect of the degree of hybridization and energy management strategy on the performance of a fuel cell/battery vehicle in real-world driving cycles. A new ammonia molten alkaline fuel cell powering system with three Rankine cycles for waste heat recovery are studied in [10]. In [11], a quantitative evaluation of the energy-saving potential of railcar battery hybridization is conducted through an optimization analysis grounded in dynamic programming. This approach is currently regarded as a highly promising solution for mitigating the greenhouse gas emissions of regional trains. Jung et al. [12] studied the hydrogen consumption of a fuel cell hybrid tram by optimizing the energy distribution between the fuel cell stack and the energy storage system. The authors of that study proposed a practical control map derived from a simulation model and based on the equivalent consumption minimization strategy, which accounts for the characteristics of both fuel cells and batteries. Yang and colleagues [13,14] investigated an optimization energy management strategy, considering the speed profile of a hybrid light rail system. This system is powered by catenary, a battery pack, and an ultra-capacitor. The objective was to explore energy-saving potential and optimize the energy management strategy. Song et al. [15] proposed a new energy management strategy that can ensure real-time operation and highly efficient energy utilization in fuel cell hybrid electric vehicles. In [16], the authors investigated optimal hybrid configurations for retrofitting a platform supply vessel using fuel cells and batteries to minimize CO_2 emissions and battery degradation. Moreover, several studies have highlighted the limitations of hydrogen systems when

used in stand-alone systems, particularly due to their slow start-up and poor performance under rapid load variations [17–20]. To address these issues, the integration of on-board Energy Storage Systems (ESSs)—mainly supercapacitors and lithium-ion batteries—is being implemented in rail applications [21]. These ESS configurations are generally customized to meet the specific operational requirements of each train type [22]. However, the process of charging the battery is contingent upon the utilization of grid electricity, a factor that has the potential to influence several key metrics, including but not limited to vehicle weight, capital investment, and maintenance costs, in a manner that is dependent on the battery size [23,24]. Therefore, the prospect of a train powered exclusively by batteries appears to be a non-viable solution.

To overcome the challenges identified and to facilitate the development of viable autonomous energy systems, there is an increasing tendency to consider hybrid architectures combining hydrogen fuel cells and batteries. From September 2018 onwards, a number of pilot projects were carried out in several European countries (e.g., Germany [25], UK [26], France [27] and Italy [28]) to test the capabilities of hybrid trains on non-electrified lines. Presently, hydrogen fuel cells and battery systems represent the most widely adopted technologies for low-carbon power generation in rail applications. Fuel cell-based systems offer high energy density, rapid refueling capabilities, and operational performance comparable to diesel locomotives, making them particularly suitable for non-electrified routes extending up to 1000 km. When powered by green hydrogen, these systems enable zero-emission mobility, with water as the sole by-product. However, dedicated infrastructure is required for refueling, as well as periodic cell replacement every 3 to 6 years, depending on usage conditions [29]. Conversely, battery-powered systems are better suited for shorter distances, typically up to several dozen kilometers, and for operations characterized by highly variable load profiles. Together, these systems form a synergistic hybrid architecture capable of addressing the operational challenges of modern rail transport, offering both efficiency and flexibility [30].

The present study aims at simulating and analyzing the behavior of a hybrid fuel cell–battery train under different powertrain configurations and route conditions, with the aim of identifying the effect of sizing parameters and routes on system performance and lifecycle costs. The novelty of this work lies in the integration of detailed component degradation models and cost evaluation within a dynamic simulation framework, enabling a techno-economic assessment of different design scenarios. Unlike most previous studies that focus on fixed configurations or average consumption estimates, the proposed approach provides a time-resolved energy analysis accounting for both hydrogen and battery dynamics, degradation phenomena, and specific route characteristics.

The paper is structured as follows: Section 2 presents the hybrid train configuration, detailing the models implemented for the powertrain components, for vehicle dynamics, energy management strategy and to account devices degradation phenomena. Section 3 describes the train typology and the simulated routes and explains the performed simulation campaign. Section 4 discusses the main results, highlighting the performance of the hybrid system under various operating scenarios and finally, Section 5 draws conclusions and offers insights into future developments and optimization strategies for hydrogen-powered hybrid trains.

2. Models

The simulation framework developed in this study is designed to assess the performance of a hybrid fuel cell–battery train over real-world railway routes. A complete numerical tool is realized allowing the simulation of the dynamic behavior of hybrid trains

based on hydrogen and batteries propulsion to test different scenarios. The programming environment is MATLAB R2024b.

2.1. Powertrain and Simulation Software Rationale

Figure 1 illustrates the architecture of the hybrid fuel cell–battery powertrain considered in this study. The system integrates two main energy sources: a hydrogen fuel cell system and a lithium-ion battery pack, both connected to a common DC-bus through dedicated DC/DC converters. The hydrogen is stored onboard in high-pressure tanks and fed into the fuel cell. The battery pack supports both motoring and regenerative braking operations. The DC-bus acts as the central node of the power system, distributing energy to the main traction unit via a DC/AC inverter that powers the electric motor. It also supplies electricity to onboard auxiliaries such as lighting, HVAC, and control systems. The overall energy flow and control logic are managed by a supervisory Energy Management System (EMS), which dynamically allocates power between the fuel cell and the battery based on real-time operational requirements and system constraints.

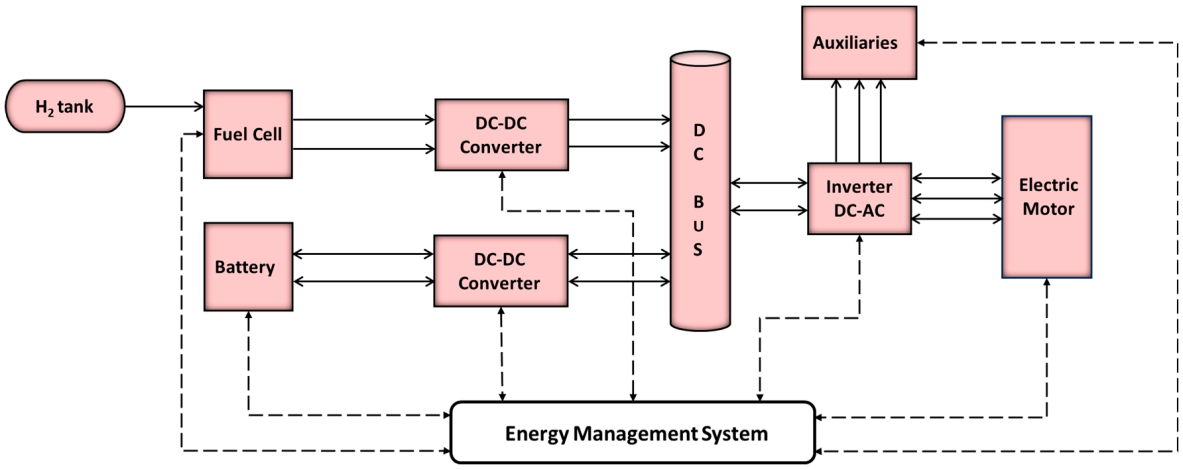


Figure 1. Powertrain block scheme.

The simulation process begins with the identification of all relevant parameters concerning the track and the train. This includes details about the route (such as length, gradient, track type, station distances) and specific characteristics of the train (such as weight, including fixed and variable components, and engine characteristics). These inputs are essential for initializing the problem and setting the foundation for subsequent calculations.

The distribution of power between the hydrogen fuel cell and the battery pack is regulated by two independent variables, namely m and n, which are used to define the system sizing:

$$power\ ratio\ (m) = \frac{P_{max,FC}}{P_{max,el}} \quad (1)$$

$$energy\ ratio\ (n) = \frac{E_{batt}}{E_{tot,batt}} \quad (2)$$

The first independent variable, m, represents the ratio between the maximum power of the fuel cell ($P_{max,FC}$) and the maximum power that electric motor can provide ($P_{max,el}$), and can vary between 0 and 1: if m equals 0, the propulsion system has no fuel cells, while if m equals 1, the fuel cells completely cover the power peak. The second variable, n, represents the energy of the installed battery (E_{batt}) in comparison with the total energy ($E_{tot,batt}$) the battery requires to guarantee a single discharge cycle during the entire trip. This parameter is used to adjust the size of the battery: if n equals 1, the battery is at its maximum size.

The selection of a value lower than 1 is possible because (partial) charges were possible due to regenerative braking and use of PEMFC (Proton Exchange Membrane Fuel Cell). The $E_{tot,battery}$ can be known after solving train dynamics in unladen weight conditions. Then, an iterative routine is run to perform a sizing calculation for the battery pack, fuel cell stack, and hydrogen storage. This step ensures that the components are appropriately sized to meet the train power and energy demands throughout the journey. With the mechanical and electrical power demand curve established, a dynamic simulation of the train journey along the specified path is conducted. This simulation calculates energy flows, battery state of charge (SOC), and hydrogen consumption at each simulation timestep, providing a detailed understanding of how the train energy systems perform under various conditions.

Finally, the cost per kilometer of the route is computed, accounting for both capital and operational costs. These include the purchase of components such as fuel cells, batteries, hydrogen storage systems, and the electric motor, as well as costs related to hydrogen consumption, battery usage, and component (FC and battery) replacements due to degradation. The developed simulation tool thus enables an effective evaluation of the system performance and cost-efficiency, supporting informed decisions in the sizing and configuration of hybrid hydrogen-powered trains.

Based on these inputs, the model performs a detailed simulation of train kinematics and dynamics, as explained in Section 2.1. From the resulting motion profile, the mechanical (P_{mech}) and electrical (P_{demand}) power curves are calculated, including the auxiliary loads (P_{aux}).

$$P_{demand} = P_{mech} \cdot \eta_{mot} \cdot \eta_{inv} \cdot \eta_{convr} + P_{aux} \ [\text{kW}] \tag{3}$$

With η_{mot}, η_{inv}, η_{conv} representing the electric motor, inverter, and converter efficiencies, respectively. According to [31], the overall efficiency of the motor and gearbox depends on the driving cycle under consideration. In cases of significant variations in power and torque, the average value is approximately 80%. The efficiency of switching devices and DC-DC and DC-AC converters, and inverters can reach values higher than 90%. In summary, an electric powertrain can ensure efficiency levels ranging from approximately 72% to 77%. For simplicity in the present simulation, constant average efficiencies were assumed: 0.80 for the electric motor, 0.95 for the inverter, and 0.95 for the DC-DC converters. These assumptions correspond to an overall efficiency of the electric transmission chain of approximately 72.2%, in accordance with what reported in [31]. In Equation (3), the power of the auxiliaries P_{aux} is assumed to be constant and equal to 200 kW.

2.2. Train Dynamic Equation

The propulsion of a vehicle requires a motor to provide energy for movement, with a drivetrain that transmits the force enabling motion. In analyzing vehicle dynamics, three main categories of forces must be considered: active forces, such as traction or braking, which act in the direction of the vehicle velocity during traction or in the opposite direction during braking, and are typically generated by onboard systems or by external towing vehicles; passive forces, which always oppose the direction of motion and arise only when the vehicle is moving; and mass-dependent forces, which include the vehicle weight, inertial forces during acceleration or deceleration, and centrifugal forces experienced along curved trajectories.

Assuming the vehicle as a rigid body or a single point, the traction force must overcome resistances and produce acceleration according to the general motion equation [24], which writes:

$$T(v) = R_{tot}(v) + m_v \cdot (1 + \beta) \cdot \frac{dv}{dt} \tag{4}$$

Here, the difference between active and passive forces must equal the inertial forces. In this formulation, $T(v)$ represents the traction force, i.e., the net result of all active forces; $R_{tot}(v)$ is the total resistance to motion; m_v is the vehicle mass; $m_v \cdot (1+\beta) = m_e$ is the equivalent mass accounting for additional force requirements; β is the mass augmentation coefficient for rotating or translating masses, which is especially relevant in heavy vehicles such as buses, trucks, and trains; and $I = m_v \cdot (1+\beta) \cdot \frac{dv}{dt}$ expresses the inertial force. The power required for vehicle motion is the product of traction force and velocity:

$$P(v) = T(v) \cdot v \tag{5}$$

The ordinary and the grade resistance forces are here considered in the calculation of the R_{tot}. Ordinary resistances R_{ord} include aerodynamic resistance, resistance at rail joints (caused by the elastic bending of the rail ends and the impact of the wheel as it moves from one rail to the next), and resistance due to hunting motion (since the movement of railway vehicles on tracks is not perfectly linear). The sum of these resistances constitutes the total ordinary resistance, which is typically estimated using a semi-empirical trinomial formula, i.e., the Davis equation [32,33]:

$$R_{ord} = m_v \cdot \left(a + b \cdot v + c \cdot v^2\right) \tag{6}$$

where the coefficients a, b, c are empirical values (known as Davis coefficients) used to calculate ordinary resistance.

Accidental resistances can be classified into three main types, inertial resistance, grade resistance and curve resistance. Inertial resistance arises from any change in velocity, while grade resistance R_{gra} depends on the altitude profile of the track, as the gradient determines the forces resulting from the weight component along the direction of travel. Considering a vehicle with a weight force P applied at its center of gravity, when the track has a certain slope, the weight force P can be decomposed into two components, parallel and normal to the track. If the gradient is positive (uphill), the parallel component opposes the motion, representing a resistance that must be overcome. Conversely, if the gradient is negative (downhill), the parallel component aids the motion. Grade resistance can be calculated using the following formula:

$$R_{gra} \approx m_v \cdot g \cdot i \tag{7}$$

where i is the gradient (expressed in [‰], i.e., the slope value multiplied by 1000). In railway applications, due to limited wheel-rail adhesion, gradients exceeding 30–35 ‰ are typically not feasible.

A standard cycle consists of two phases. The first one corresponds to the Stop phase, characterized by zero velocity and absence of active and passive forces. The second one is when the train is moving, which is defined by non-zero velocity, with active and passive forces that vary depending on the phase of motion. Movement occurs between two stop phases and requires at least two periods of variable velocity: an acceleration phase (starting) and a deceleration phase (braking). The four main phases of movement are acceleration, cruise, coasting and braking. If the cruise and coasting phases are absent, the cycle is referred to as a "reduced cycle", otherwise, it is considered a "full cycle". Table 1 describes each phase based on the values of terms in the fundamental motion equation.

Table 1. Train movement phases and associated velocity, acceleration and forces.

State	Phase	Velocity	Acceleration	Forces
Stop	/	$v = 0$	$\frac{dv}{dt} = 0$	$T = 0$ $R_{tot} = 0$ $I = 0$
Movement	Acceleration $T - R = m_e \cdot \frac{dv}{dt}$	$v \neq 0$	$\frac{dv}{dt} > 0$	$I < 0$ $R_{tot} < T$
	Cruise $T - R = 0$	$v = cost$	$\frac{dv}{dt} = 0$	$I = 0$ $R_{tot} = T$
	Deceleration $-R = m_e \cdot \frac{dv}{dt}$	$v < 0$	$\frac{dv}{dt} < 0$	$T = 0$ $R_{tot} = I$
	Braking $-T - R = m_e \cdot \frac{dv}{dt}$	$v < 0$	$\frac{dv}{dt} < 0$	$I > 0$ $R_{tot} \neq 0$

2.3. FC Model

The fuel cell system implemented in this study is based on a low-temperature PEMFC, chosen for its high efficiency, fast start-up time, and suitability for mobile applications. The model is designed to dynamically simulate the electric and hydrogen performance of the fuel cell under varying load conditions, reflecting the transient power demands of railway operation. The model is based on the approach presented in [34].

Each fuel cell stack consists of n_{cells} individual cells, connected in series. The stack voltage V_{FC} is computed as:

$$V_{\mathrm{FC}} = n_{\mathrm{cells}} \cdot V_{\mathrm{cell}} \tag{8}$$

where V_{cell} is the cell voltage.

The single-cell voltage is calculated by subtracting the main irreversible losses from the theoretical open-circuit potential $\overline{\mathrm{E_{id}}}$ about 1.17, following:

$$V_{\mathrm{cell}} = \overline{E_{\mathrm{id}}} - \Delta V_{\mathrm{act}} - \Delta V_{\mathrm{ohm}} - \Delta V_{\mathrm{conc}} \tag{9}$$

where ΔV_{act}, ΔV_{ohm} and ΔV_{conc} are the activation, ohmic and concentration losses, respectively. Each loss is computed through a semi-empirical equation.

Activation losses follow:

$$\Delta V_{\mathrm{act}} = \frac{R \cdot T}{z \cdot F} \cdot \ln\left(\frac{I_{\mathrm{dens}}}{I_{\mathrm{dens},0}}\right) \tag{10}$$

Ohmic losses are modeled as:

$$\Delta V_{\mathrm{ohm}} = (R_{\mathrm{ohm}} + k_s) \cdot I_{\mathrm{FC}} \tag{11}$$

Concentration losses are considered negligible in the operating range considered.

The electric power output is then:

$$P_{\mathrm{FC}} = V_{\mathrm{FC}} \cdot I_{\mathrm{FC}} \tag{12}$$

While hydrogen consumption is estimated from Faraday's law as:

$$\dot{m}_{\mathrm{H_2}} = \frac{I_{\mathrm{FC}} \cdot n_{\mathrm{cells}} \cdot n_{\mathrm{stack}} \cdot MW_{H2}}{2 \cdot F \cdot 1000} \tag{13}$$

where $MW_{H2} = 2$ kg/kmol is the molar mass of hydrogen. Finally, the fuel cell efficiency is computed as:

$$\eta_{\mathrm{FC}} = \frac{P_{\mathrm{FC}}}{\dot{m}_{\mathrm{H_2}} \cdot LHV_{H2} \cdot 10^3} \tag{14}$$

With $LHV_{H2} = 120$ MJ/kg.

The fuel cell operates in the range between its idling power and a defined upper limit. A nonlinear solver is used to determine the operating point (V, I) for a given power request. The polarization curve is dynamically reconstructed through iterative inversion of the voltage-current relationship, using a function embedded in the simulation code. The PEMFC is modeled at a nominal temperature of 343.15 K and 3 bar operating pressure, with an active area of 500 cm^2 per cell and a membrane thickness of 183 µm. The model parameters were calibrated based on experimental and literature data [34].

2.4. Battery Model

The battery system implemented in this study is based on lithium iron phosphate (LFP) technology, widely adopted in mobility applications due to its high safety, long cycle life, and good power performance. The battery pack is composed of electrochemical cells connected in series and in parallel to form strings and modules. Cells connected in series increase the total voltage, while parallel connections increase capacity. The battery model used in this study recalls the "Battery Equivalent Circuit" block provided by Simscape [35]. The total battery voltage and capacity are computed as:

$$V_{\mathrm{tot}} = V_{\mathrm{batt,cell}} \cdot n_{\mathrm{bat,cell}}; \quad C_{\mathrm{tot}} = C_{\mathrm{string}} \cdot n_{\mathrm{string}} \tag{15}$$

Each string is characterized by its own open-circuit voltage (V_{OC}), internal resistance, and SOC. The total battery resistance is computed from the parallel combination of the individual string resistances, and a nonlinear solver is used to determine the operating point based on power request and electrical constraints.

The current through the equivalent battery circuit is computed as:

$$I_{\mathrm{OC}} = \sum_{i=1}^{n_{\mathrm{strings}}} \frac{V_{\mathrm{OC},i}}{R_{\mathrm{string},i} + R_{\mathrm{wire},i}} \tag{16}$$

$$R_{\mathrm{bat,tot}} = \left(\sum_{i=1}^{n_{\mathrm{strings}}} \frac{1}{R_{\mathrm{string},i} + R_{\mathrm{wire},i}} \right)^{-1} \tag{17}$$

Hence, a system of equations is solved to obtain the terminal voltage V_{batt} and the battery current I_{batt}:

$$P_{\mathrm{batt}} = V_{\mathrm{batt}} \cdot I_{\mathrm{batt}}; \quad V_{\mathrm{batt}} = I_{\mathrm{OC}} \cdot R_{\mathrm{bat,tot}} - I_{\mathrm{batt}} \cdot R_{\mathrm{bat,tot}} \tag{18}$$

Once the operating point is defined, the current of each string is determined as:

$$I_{\mathrm{string}} = \frac{V_{\mathrm{OC}} - V_{\mathrm{batt}}}{R_{\mathrm{string}} + R_{\mathrm{wire}}} \tag{19}$$

The state of charge of each string is then updated by integrating the current over time, using Coulomb counting:

$$\mathrm{SOC}_{\mathrm{string}} = \mathrm{SOC}_{\mathrm{string},0} - \frac{I_{\mathrm{string}} \cdot \Delta t}{C_{\mathrm{string}}} \tag{20}$$

The battery model also updates internal parameters dynamically, including the open-circuit voltage and internal resistance, based on SOC and temperature. Heat generation due to Joule losses is computed and used to update cell temperature, which affects wire resistivity and string resistance. These aspects allow the model to reflect real battery behavior under varying operational and thermal conditions.

2.5. Storage System

The hydrogen storage system considered in this work is based on high-pressure gas tanks, which currently represent the most widespread solution for onboard storage in rail mobility applications. The storage pressure is fixed at 350 bar. The storage model is based on the ideal gas law and calculates the pressure variation in the tank according to the net volumetric balance of hydrogen inflow (from an electrolyzer, if present) and outflow (mainly toward the fuel cell). The working logic is summarized by the following equations.

The first step is to compute the volume variation due to the hydrogen required by the fuel cell:

$$\Delta vol = -H_{2,\text{requested}}/\rho_{H2} \tag{21}$$

Assuming ideal gas behavior, the pressure variation in the tank is estimated from:

$$\Delta p = \frac{R \cdot T \cdot \Delta vol}{vol_{\text{storage}} \cdot f_{conv}} \tag{22}$$

where $R = 8.314\ \text{J}/(\text{mol}\cdot\text{K})$ is the universal gas constant, T is the absolute temperature (in K), and the denominator accounts for the molar volume adjustment (from mol to Nm^3).

The final pressure is calculated by adding the pressure variation (Δp) to the current value:

$$p_{\text{fin}} = p_{\text{in}} + \Delta p \tag{23}$$

The normalized storage level (ranging between 0 and 1) is then given by:

$$\text{NL} = \frac{\text{p}_{\text{fin}}}{\text{p}_{\text{max}}} \tag{24}$$

This model dynamically updates the pressure and level of the tank at each timestep of the simulation and ensures that safety constraints are respected. A persistent variable approach is used to track the tank state over time, consistent with the discrete-time logic of the simulation.

2.6. Energy Management System

In the present study, a rule-based EMS developed by the authors is employed. A rule-based energy management system is a control strategy that governs the distribution of energy in a hybrid system by implementing predefined rules in accordance with operating conditions and set thresholds. The primary objective of the EMS is to reduce hydrogen consumption and FC derating phenomena by trying to make the FC work close to its nominal power ($P_{nom,FC}$). In fact, the FC operational limits are defined by upper ($P_{upper,FC}$) and lower ($P_{lower,FC}$) thresholds, set at 105% and 95% of its nominal power output, respectively. During high power demand periods, the EMS sets the fuel cell power at the upper limit. In this state, the battery system assists the fuel cell in supplying power to the motor and auxiliary load. On the other hand, when the required power is below the upper threshold of the fuel cell, the battery system is shut down and the fuel cell system supplies the entire load. To prevent excessive power fluctuations, which cannot be compensated due to the slower dynamics of the fuel cell, this state is maintained only if the requested power remains within the lower and upper limits of the fuel cell. If the requested power falls

below this range, the fuel cell goes idling ($P_{idling,FC}$), and the motor load is entirely covered by the battery system if its SOC conditions permit it. In all these conditions, the fuel cell is never used for battery charging; only regenerative braking is used during deceleration. The only exception is when the battery state of charge falls below 30%. In that state, the fuel cells power is set to the maximum ($P_{max,FC}$) allowable threshold of 110% of the nominal power, and the fuel cell is used to recharge the battery when possible.

2.7. Degradation Models

It is an established fact that, during their operational life, devices such as batteries, fuel cells, inverters and converters undergo a process of degradation that has a detrimental effect on their performance on an annual basis. In certain instances, the decline in performance is deemed to be negligible; in others, however, it is not. It is imperative that devices are replaced at regular intervals as they deteriorate, to maintain optimal functionality and reduce overall system costs. In the present study, the performance degradation of the main devices, namely FC and battery, is considered to achieve this aim.

2.7.1. PEM Fuel Cell

In real-world mobility applications, PEMFCs operate under diverse environmental conditions, including fluctuating humidity and temperature levels [36], which significantly influence their efficiency and durability. Performance degradation can be triggered by several factors, such as suboptimal water and thermal management, gas starvation, contamination, and frequent load variations [37]. Notably, repeated load cycling promotes the agglomeration of platinum particles within the cathode catalyst layer, thereby reducing the electrochemically active surface area. This effect is more pronounced on the cathode side due to the higher electric potential at the membrane–cathode interface compared to the anode. Furthermore, these voltage fluctuations can accelerate carbon support corrosion and compromise the integrity of both the membrane and the gas diffusion layers [38], increasing the likelihood of irreversible performance losses.

Several studies have examined how different operating modes affect FC stack durability, highlighting the significant impact of real-world conditions on degradation phenomena [39,40]. Among them, Zhao et al. [41] conducted an in-depth analysis of FC performance decay using experimental data from actual road tests on a bus operating in China. The authors derived a semi-empirical formula to estimate the system lifetime based on load profiles observed during the tests. Their findings indicate that under intermittent and highly variable load conditions, typical of urban mobility, the fuel cell lifespan is limited to approximately 5000 h. Conversely, under continuous operation at a fixed load point, the expected lifetime can increase up to 30,000 h. This clearly shows that degradation is strongly influenced by the operational profile of the vehicle, particularly by start–stop events, idling phases, abrupt load changes, and periods of sustained high-power demand. Zhao et al. also developed a model capable of quantifying the impact of each of these conditions, and this model has been adopted as a reference framework in the present study. For clarity, a summary of the key features of the degradation model is provided below, while full details can be found in the original publication.

To assess fuel cell degradation under real operating conditions, each driving cycle can be characterized by the contribution of four distinct behavioral modes:

$$Driving\ Cycle\ =\ f\{n_1,\ t_1,\ n_2,\ t_2\} \tag{25}$$

where f denotes a general function capturing the impact of these parameters on the overall cycle. Specifically, n_1 represents the average number of start–stop events per hour, while t_1 denotes the mean duration spent idling within the same timeframe. n_2 accounts for the

average frequency of load change events per hour, and t_2 corresponds to the average time spent operating at high power. These four operating conditions are illustrated schematically in Figure 2, which outlines a typical fuel cell duty cycle and highlights the transitions between the different phases.

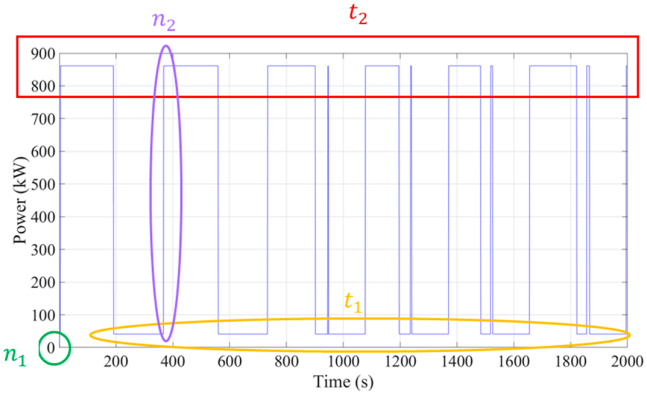


Figure 2. Key operational factors influencing fuel cell degradation illustrated over a representative working cycle.

In their study, Zhao et al. [41] experimentally quantified the voltage degradation associated with each operating phase of a typical driving cycle. The resulting degradation rates are summarized in Table 2. Based on these findings, the overall voltage decay rate V_{deg}, is calculated as the weighted sum of the individual contributions:

$$V_{deg} = n_1 V_1 + t_1 U_1 + n_2 V_2 + t_2 U_2 \quad (26)$$

where V_1, U_1, V_2 and U_2 represent the degradation contributions (in V/h or V/cycle) of start–stop events, idling, load change, and high-power phases, respectively.

Table 2. Experimentally observed weighting factors for voltage degradation in PEM fuel cells under different operating conditions [42].

Operating Conditions	Voltage Degradation Rate
Start–Stop	$V_1 = 13.79$ μV/cycle
Idling	$U_1 = 8.662$ μV/h
Load Change	$V_2 = 0.4184$ μV/cycle
High power load	$U_2 = 10.00$ μV/h

Given a predefined threshold for allowable voltage drop per cell, ΔV, the estimated fuel cell lifetime t_{FC} can be computed as:

$$t_{FC} = \frac{\Delta V}{k \cdot V_{deg}} \quad (27)$$

where k = 1.72 is a calibration factor introduced to align the model output with real-world degradation measurements from operating fuel cell buses. The validity of this semi-empirical model was confirmed in a follow-up study [42], where predicted and observed degradation trends showed good agreement. In the present work, this degradation model has been integrated into the dynamic simulation tool to evaluate the fuel cell lifespan across different operational scenarios.

2.7.2. Battery

The battery degradation model used in this study is based on a lithium-ion cell simulated through the generic Simulink block [43,44]. The key factors influencing battery

aging include the depth of discharge (DoD), charge/discharge rates (C-rate), and operating temperature (T_{batt}). Among these, the DoD plays a pivotal role and is defined as the fraction of capacity extracted from the battery during one cycle [45]. The associated state of charge (SoC) denotes the remaining usable capacity and is typically constrained between predefined upper and lower thresholds.

The C-rate, defined separately for charge and discharge modes, represents the ratio of actual current to the nominal capacity over a one-hour interval [46]. High C-rates lead to increased thermal stress and undesired electrochemical reactions, accelerating degradation. Although temperature is another critical factor, it is not actively controlled in this simulation; instead, efforts are made to limit current oscillations to minimize thermal excursions.

Battery degradation is quantified through the state of health (SoH), defined as the ratio of the actual capacity to the nominal initial capacity. The SoH decreases over time due to both calendar aging and cyclic aging, and the battery is considered end-of-life when SoH drops below 0.8.

The evolution of SoH is computed as:

$$SoH_{end} = SoH_{start} - \Delta SoH \tag{28}$$

$$\Delta SoH = \frac{1}{T_{life}} \cdot AGE(\Delta t) \tag{29}$$

where T_{life} is the nominal lifetime (in hours) and AGE(Δt) is a function capturing the aging over time interval Δt. The total aging function is split into two components:

$$AGE = AGE_{cal} + AGE_{cyc} \tag{30}$$

The calendar aging component depends primarily on the absolute deviation of SoC from its reference value (typically 0.5), while the cyclic aging depends on the energy exchanged in charging/discharging processes and the number of cycles, both of which are related to the DoD. Cyclic aging uses a Wöhler-type empirical model [47], which relates the number of cycles N_{cyc} to the DoD:

$$N_{cyc} = d \cdot DoD^{-j} \tag{31}$$

where d and j are technology-specific coefficients. The associated energy exchanged per cycle is:

$$E_{cyc} = P_{ch/dis} \cdot \Delta t \tag{32}$$

This approach allows a realistic tracking of SoH throughout the simulation based on the actual operating conditions. The model is aligned with findings from [47,48], and supports dynamic updates of SoH at each timestep in the hybrid simulation framework.

2.8. Economic Analysis

As an additional element of analysis, the specific cost (sc, in €/km) is calculated for all the configurations tested, i.e., the cost of traveling 1 km with the powertrain under consideration, in the configuration and on the route considered. This value is exclusively related to the powertrain, under the assumption that all other components of the train remain unchanged. The specific cost (Equation (33)) is expressed as the sum of CAPEX (Capital Expenditure), OPEX (Operative Expenditure), and replacement costs (REPLEX) divided by the annual traveled distance (in km).

$$sc = \frac{CAPEX + OPEX + REPLEX}{n_{trips,year} * dist_{trip}} \tag{33}$$

In Equation (33), the capital costs account for the installation costs of the fuel cell, battery and hydrogen tanks. In the context of operational costs, the cost of refueling hydrogen and charging batteries at the end of each journey are considered, as well as the scheduled maintenance costs, which represents the planned maintenance expenses for all the components over their lifetimes. Finally, according to the degradation model described in Section 2.7, replacement costs can be estimated, encompassing both fuel cell and battery replacement. All OPEX and REPLEX costs have been appropriately actualized.

3. Simulation Details

3.1. Reference Train Configuration and Simulations Parameters

A representative hybrid electric train typology typically used for non-electrified regional routes was selected as the basis for this study. This type of train is designed for passenger service and features both a catenary power supply and an autonomous onboard propulsion system. The train configuration considered for simulations includes four cars, with a total empty weight of approximately 165 tons, increasing to 195 tons (m_v) under full load conditions (excluding the propulsion system). The traction components are roof-mounted to maximize available space for passengers. For the development of the hybrid Fuel Cell–Battery train model (Figure 1), a train powered by an onboard diesel engine in combination with traction batteries is considered. This configuration was adopted as a reference because its architecture, based on an onboard power generation system combined with energy storage, is more consistent with the layout envisioned in this study. We assume that a hydrogen fuel cell system could replace the original diesel engine and tank through retrofitting interventions, enabling zero-emission operation while preserving the original hybrid traction scheme. The selected configuration provides a maximum wheel power of 1334 kW, a design speed of 160 km/h. The nominal mechanical power previously delivered by the diesel engine was 1435 kW. For modeling purposes, this is replaced by an electric motor with equivalent power and a typical electrical efficiency of 80% [31].

The motor dynamic performance is defined by two key characteristic curves: the traction curve and the braking curve. These curves are essential for accurately simulating the train dynamic behavior during both acceleration and braking phases as it represents the train capability to overcome resistance forces and achieve desired accelerations under different operating conditions. The traction characteristic curve $T(v)_{max}$ represents the maximum traction force that the motor can deliver to the wheels at various speeds. The curve was developed in MATLAB by interpolating a set of known data points derived from empirical measurements or manufacturer specifications, each consisting of a traction force and corresponding velocity value as illustrated in Table 3.

Table 3. Maximum traction and braking force for different velocity values of the considered electric motor [33].

Velocity [km/h]	Traction Force [kN]	Braking Force [kN]
30	160.00	
40	119.99	
50	95.98	
60	79.98	120.00
70	68.55	99.99
80	59.99	87.50
90	53.32	77.77
100	47.99	
110	43.64	63.63

Table 3. *Cont.*

Velocity [km/h]	Traction Force [kN]	Braking Force [kN]
120	39.99	58.33
130	36.91	50.00
140	34.28	46.43

The curve is constant until a velocity of 30 km/h and then decreases with velocity. Similarly, the braking characteristic curve $-T(v)_{max}$ outlines the maximum braking force (in absolute terms) that the motor can exert at different speeds. This curve is needed to evaluate the train regenerative braking potential, as it defines the maximum amount of kinetic energy that can be converted back into electrical energy during deceleration. Like the traction curve, the braking curve was constructed in MATLAB using an interpolation function applied to a set of braking force and velocity data pairs. The braking force remains null up to a velocity of approximately 8 km/h. It then exhibits a linear increase until reaching a velocity of 15 km/h, where it stabilizes at a maximum value of 120.00 kN. This constant braking force is maintained until a velocity of 57 km/h, after which it begins to decrease progressively, following the values detailed in Table 3.

The total mass of the train was considered as the sum of two components: fixed mass and variable mass. The fixed mass, amounting to 195 tons, accounts for the weight of passengers, the motor, and all carriage components. The variable mass represents the propulsion system, including the fuel cell stack, battery pack, hydrogen tank, and associated auxiliaries. The Davis coefficients a, b and c, which are required for calculating rolling resistance, were set as follows: a = 9.4 $\frac{N}{t}$, b = 0.011 $\frac{\mathrm{N}}{\mathrm{t}} \cdot \frac{\mathrm{km}}{\mathrm{h}}^{-1}$, c = 0.0029 $\frac{\mathrm{N}}{\mathrm{t}} \cdot \frac{\mathrm{km}}{\mathrm{h}}^{-2}$. These values, which are normalized by the train weight in tons, were provided by the train manufacturer and fall within the typical range reported for conventional train configurations [3]. The mass increment coefficient β was fixed at 0.05. The static adhesion coefficient f_0, necessary for calculating slip acceleration, was set to 0.33, while the adhesion ratio m_a, also used for slip acceleration, was set to 0.6. The transmission efficiency η_t, used to calculate the effective energy delivered from the motor to the wheels during motion and vice versa during braking, accounting for energy losses, was set at 0.93. To ensure passenger comfort, the maximum acceleration $a_{comfort}$ and deceleration were limited to 0.8 m/s^2. All the train-related parameters used in the simulations campaign are summarized in Table 4.

Table 4. Train main parameters used in the simulations.

Parameters	Values	Ref.
$P_{nom,mecc,mot}$ [kW]	1435	assumed
P_{aux} [kW]	200	[33]
$\eta_{trasmission}$	0.93	assumed
η_{mot}	0.8	[31]
η_{DC-DC}	0.95	[31]
$\eta_{inverter}$	0.95	[31]
$weight_{laden}$ [ton]	195	assumed
$a_{comfort}$ [m/s^2]	0.8	[33]
$dec_{comfort}$ [m/s^2]	0.8	[33]
f_0	0.33	[49]
a [N/t]	9.4	[3]

Table 4. *Cont.*

Parameters	Values	Ref.
b [(N/t)/(km/h)]	0.011	[3]
c [(N/t)/(km/h)^2]	0.0029	[3]

Lastly, unit costs and parameters used in the economic analysis are summarized in Table 5. Such parameters can be properly adjusted to adapt the simulation to different scenarios, especially in case of variation in electricity or hydrogen costs, and improved maturity of the technologies (thus reducing installation costs).

Table 5. Unit costs and parameters used in the economic analysis to calculate the total cost per kilometer of the simulated route.

Parameters	Values	Ref.
Fuel Cell Installation Cost [€/kW]	145	[50]
Battery Installation Cost [€/kWh]	100	[51]
Tank Installation Cost [€/kg H_2]	400	[52]
Scheduled Maintenance Cost [% of installation cost]	2	assumed
Electricity Cost [€/kWh]	0.19	[53]
Hydrogen Cost [€/kg H_2]	6	[54]
Actualization Rate (i)	4%	assumed
Useful Life (n) [years]	20	assumed

3.2. Simulated Routes Specifics

Three non-electrified routes were considered in this study. The first is a 16.5 km mountainous route in Piemonte, northern Italy, currently operated with Diesel traction. It was chosen as an ideal candidate for hybrid implementation due to its challenging terrain and potential for improved efficiency. The second route, Catanzaro Lido–Reggio Calabria, is significantly longer and traverses predominantly flat terrain. Lastly, the third simulated route is the Florence–Siena, is a hilly line 93.56 long [55,56]. As the three routes are in different parts of Italian peninsula, in the text they will be referred as NIL (North Italy Line), SIL (South Italy Line), CIL (Center Italy Line), respectively. Apart from the location, the three routes have different specific characteristics, and provide a good test bench to analyze the powertrain behavior under different operating conditions. The route characteristics include the altitude profile, the route length, station positions and dwell time (fixed at 120 s) and the maximum speed limits for each route segment. These features are summarized in Figure 3 and Table 6 for the three analyzed routes.

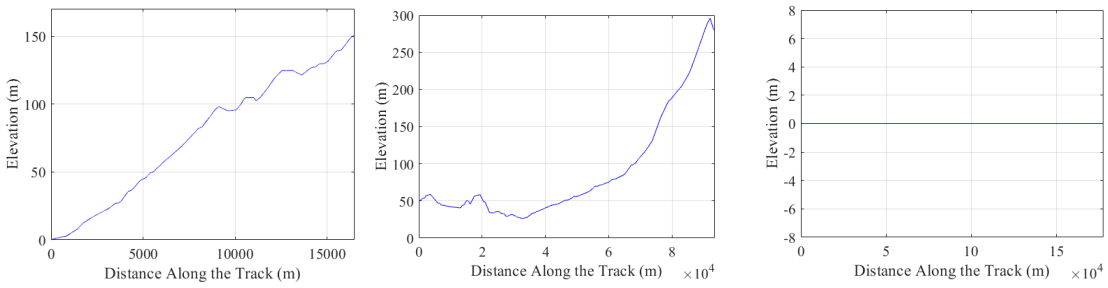


Figure 3. Elevation–distance correlation on the three routes tested: NIL (**left**), CIL (**center**), and SIL (**right**).

Table 6. Main features of the three simulated routes.

Parameters	NIL	CIL	SIL
Number of Stations	7	8	37
Route Length [km]	16.5	93.56	177.55
Speed Limits [km/h]	[90–60]	[90–120–140–105–140–100–140 –100–140–100–130–80–85]	[130]
Segment at Speed Limit [km]	[0–7.8–16.5]	[0–13,010–22,459–24,762–30,549–42,601–45,601–48, 601–54,601–58,601–68,418–81,601–93,559]	[0–177.55]
Stopping Time (s)	120	120	120
Dwell Time (s)	300	300	300
Average Gradient	9‰	2.6‰	0‰
Maximum Gradient	23.8‰	12.36‰	0‰

3.3. Simulation Campaign

To evaluate the performance and behavior of the hybrid powertrain under different operating conditions, a comprehensive simulation campaign was carried out. The analysis focused on two main aspects: the sensitivity of the system sizing parameters and the influence of different railway routes.

First, a sensitivity analysis was conducted on the reference route SIL by varying the two independent design parameters of the powertrain sizing algorithm:

- m, the variable controlling the share of power covered by the fuel cell;
- n, the battery capacity ratio.

These two parameters were varied independently to evaluate their influence on key performance indicators such as battery cycling behavior, energy consumption and total cost. The SIL route is taken as reference because it is the longest one and the one with no altimetric variation, allowing to better understand the effect of m and n variations.

In the second stage of the simulation campaign, the configuration with m = 0.45 and n = 0.2 was tested on three different railway routes: SIL (baseline), CIL (characterized by more frequent stops and variable gradients), and NIL (a short route with high-power transients). This allowed us to assess the impact of route-specific features on the overall system performance, while maintaining a constant powertrain configuration. All the simulations consider round journey to exclude a different altitude at the start and end station.

Table 7 summarizes the configuration of each simulation, while the results are presented and discussed in Section 4.

Table 7. Summary of the different cases simulated to assess the performance of a hybrid FC–battery train, with the respective FC and battery main characteristics.

Simulation	Route	m	n	P_{FC} (kW)	E_{batt} (kWh)
m-1	SIL	0.40	0.10	729. 2	681.1
m-2	SIL	0.45	0.10	820.3	631.4
m-3	SIL	0.50	0.10	911.5	585.0
n-1	SIL	0.45	0.05	820.3	315.7
n-2	SIL	0.45	0.10	820.3	631.4
n-3	SIL	0.45	0.15	820.3	947.1
n-4	SIL	0.45	0.20	820.3	1262.8
route-1	NIL	0.45	0.20	820.3	114.8
route-2	CIL	0.45	0.20	820.3	408.1
route-3	SIL	0.45	0.20	820.3	1262.8

4. Results and Discussion

As anticipated, a simulation campaign was carried out to analyze the influence of the main factors on the system performance. In particular, the effect of m, n and of the route have been studied. In the following subsections results are reported and discussed.

4.1. Effect of Varying FC Power Ratio (m)

Figure 4 illustrates the power distribution between the fuel cell (FC) and the battery, along with the battery state of charge (SOC), for different values of the power ratio parameter m (simulations m-1, m-2, and m-3 in Table 7). The power plot is showed for the first 6000 s only to better highlight the behavior of the energy sources under the implemented EMS. As m increases, the nominal power of the fuel cell also increases (Figure 4-left, yellow lines), allowing it to contribute more significantly to both supplying traction power and recharging the battery.

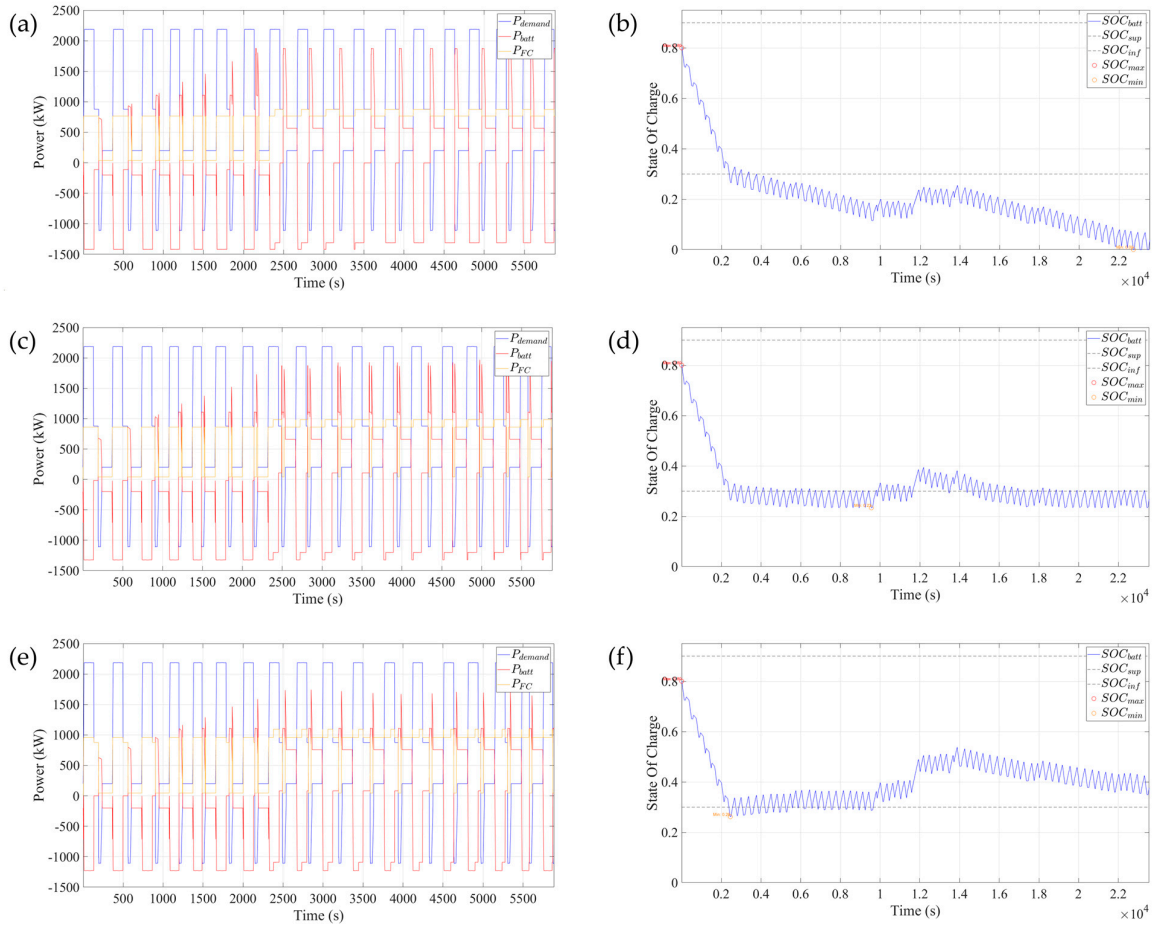


Figure 4. Power (**a**,**c**,**e**) and state of charge of the battery (**b**,**d**,**f**) for m = 0.4, 0.45, 0.5 (from top to bottom; simulations m-1, m-2, and m-3, respectively).

Figure 5 complements this analysis by showing the operating time of the battery and the FC, as well as their specific energy consumption (expressed in kWh/km). A higher m leads to a longer battery charging phase and a shorter discharging phase. In particular, when m reaches 0.5, the FC becomes powerful enough to restore the battery SOC above its lower threshold once it drops below the minimum level. From that point onward, regenerative braking alone is sufficient to keep the SOC above the critical limit, and the FC is no longer required for battery recharging. As a result, both the FC operating time and

the battery cycling (charging/discharging durations) are reduced. This ultimately leads to a decrease in specific energy consumption for both components.

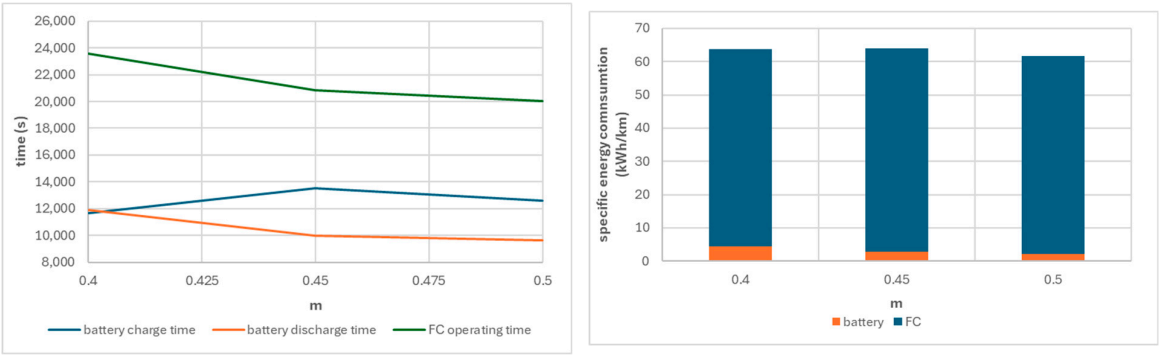


Figure 5. Operating time (**left**) and specific energy consumption (**right**) as a function of m.

The battery-specific energy consumption (Figure 5-right) shows a decreasing trend as m increases, despite the longer charging times. This behavior is associated with a higher final SOC, suggesting that the overall energy delivered by the battery is reduced. On the other hand, the fuel cell specific consumption initially increases slightly, as the FC supports battery recharging more actively. However, as m continues to grow and the FC is used less for recharging (due to sufficient regenerative braking), its specific consumption decreases. Overall, the total specific energy consumption decreases with increasing m, with the reduction in FC consumption representing the dominant contribution to this improvement.

The variation in the power ratio m also affects the degradation behavior of both the fuel cell and the battery. Table 8 summarizes the number of replacements required over a 20-year service life, along with the most relevant degradation indicators from the FC and battery model described in Section 2.7. As m increases, the number of battery replacements rises from 6 to 7, reflecting greater cycling activity. To further interpret this trend, a cycle counting analysis was performed on the battery state-of-charge (SOC) profiles using the Rainflow method [57], which is commonly employed to estimate fatigue life and cycle-based degradation in batteries. The results, included in Table 8, show that the equivalent number of full cycles slightly increases with m, from 4.54 to 4.95, despite the fact that the minimum SOC also increases (indicating that the battery is less deeply discharged). This is explained by the persistently high depth of discharge (DoD) per cycle (always above 0.96), and by the fact that, although the SOC does not drop as low, the battery continues to experience frequent and deep charge/discharge cycles, which still accelerate aging. Fuel cell replacements also increase, but they reach a peak at m = 0.45. This non-monotonic trend can be explained by examining the number of load variation cycles per kilometer, which—after ON/OFF cycling frequency—represents the most critical factor contributing to FC degradation. As such, the number of FC replacements follows the same trend as this degradation metric.

The combined effects of system behavior, component degradation, and associated investment, operational, and replacement costs determine the overall cost per km for each simulated configuration. This total cost, expressed in €/km, serves as a comparative metric. As shown in Figure 6, keeping the battery energy ratio n constant and varying the FC power ratio m produces a non-monotonic cost trend. At m = 0.40, both the fuel cell and the battery require the fewest replacements (5 and 6, respectively), resulting in the lowest total cost of about 4.0 €/km. However, this configuration is not technically viable on the SIL route: as shown in Figure 4b, the SOC repeatedly falls below the minimum admissible threshold (0.3)

and even reaches zero near the end of the mission, which would compromise operational continuity. Therefore, the associated cost cannot be considered representative.

Table 8. Summary of the degradation indicators and component replacements in 20 years for both the fuel cell (FC) and the battery, as a function of *m*.

FC Degradation Parameters	***m* = 0.40**	***m* = 0.45**	***m* = 0.50**
Idling time per hour (s/km)	1149	2717	3547
Time of the high-power load operation (s)	22,400	20,832	20,008
Number of ON/OFF cycles per km	1	1	1
Number of cycles at variable load per km	166	394	358
# of FC replacements in 20 years	5	8	7
Battery degradation parameters	***m* = 0.40**	***m* = 0.45**	***m* = 0.50**
SOC_{min}	0.000	0.233	0.262
Equivalent cycles	4.54	4.64	4.95
Average DoD per cycle	0.986	0.960	0.988
# of battery replacements in 20 years	6	6	7

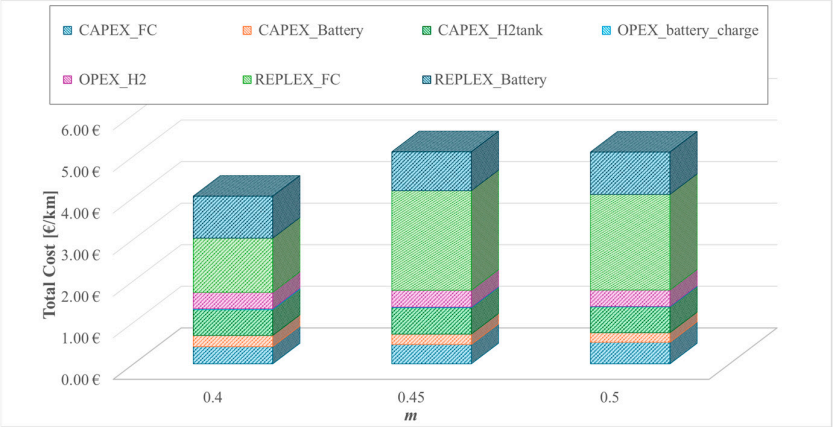


Figure 6. Breakdown of total costs as a function of the fuel cell power ratio (m). Each stacked bar reports the contribution of annualized CAPEX (fuel cell, battery, hydrogen tanks), OPEX (hydrogen consumption, charging electricity), and replacement costs (fuel cell and battery).

At *m* = 0.45, the number of battery replacements remains unchanged, but fuel cell replacements rise to 8, leading to the highest total cost of about 5.1 €/km. When *m* increases to 0.50, fuel cell replacements decrease slightly (7 instead of 8), but this improvement is offset by one additional battery replacement (7 instead of 6), resulting in a nearly unchanged total cost of about 5.1 €/km. Figure 6 clearly shows that the increase from *m* = 0.40 to 0.45 is mainly driven by higher FC replacement costs (REPLEX_FC), while OPEX contributions (hydrogen and charging electricity) remain relatively small in all cases. This confirms that, under the assumed energy prices, component degradation and replacement dominate the lifecycle cost. Overall, the analysis suggests that *m* = 0.50 offers a marginally better trade-off than *m* = 0.45, but that lower values of *m*—although more cost-effective—are not viable without revising the EMS or oversizing the battery.

4.2. Effect of Varying Battery Capacity (n)

Figure 7 shows the power distribution (plots a, c, e, g) and battery SOC evolution (plots b, d, f, h) for different values of the energy sizing parameter *n* (simulations *n*-1, *n*-2, *n*-3, and *n*-4 in Table 7). As in the previous section, the power distribution is displayed only for the first portion of the route. Figure 8 presents the battery and FC operating times (left) and the specific energy consumption (right) as functions of *n*. As *n* increases, the

battery capacity also increases, leading to a greater contribution from the battery in meeting the power demand (Figure 7a,c,e,g—red line). As a result, the battery discharges more slowly, reaches the minimum SOC later, and ends the mission with a higher final SOC (Figure 7b,d,f,h). Consequently, as n increases, the battery charging time tends to decrease while the discharging time increases (Figure 8-left).

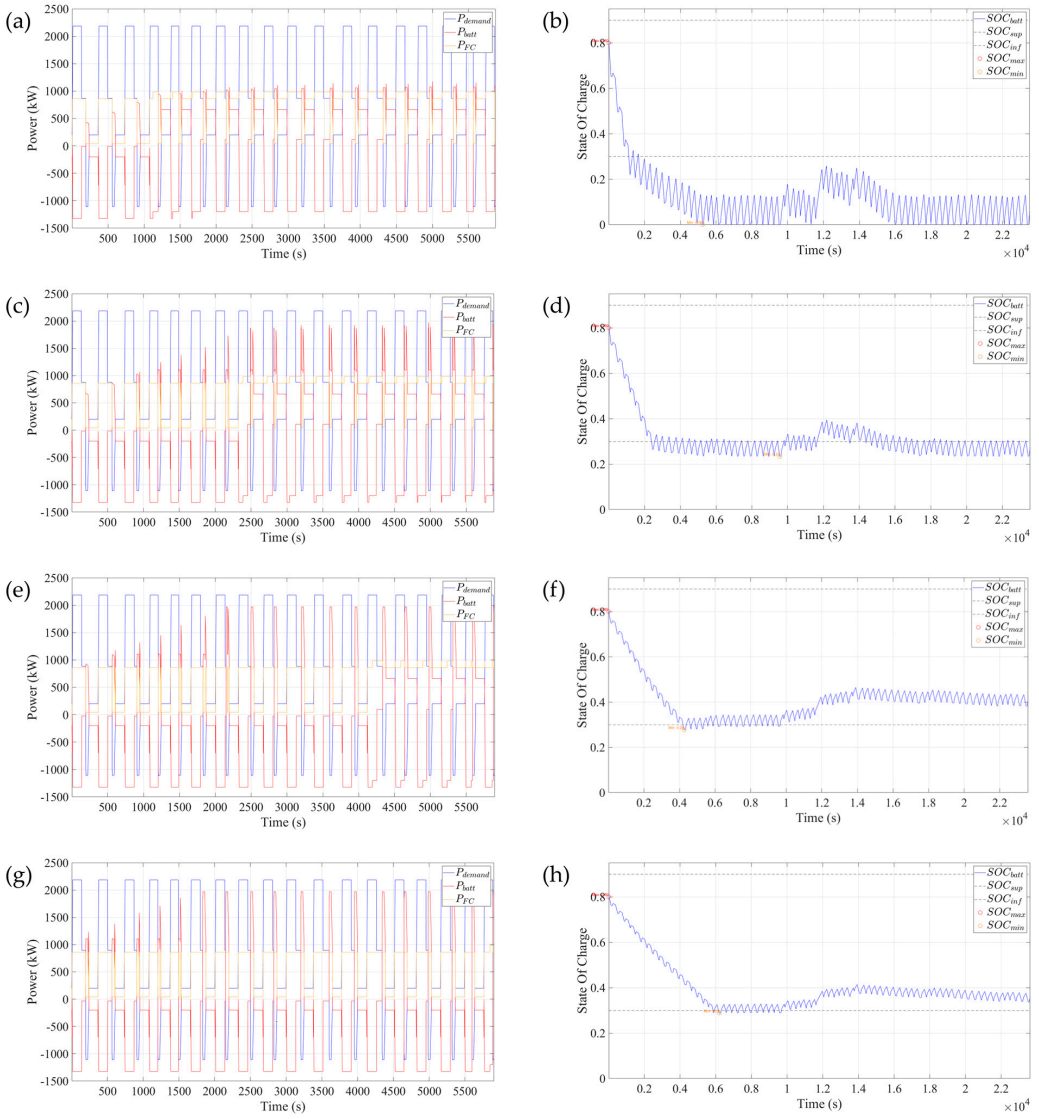


Figure 7. Power (**a**,**c**,**e**,**g**) and state of charge of the battery (**b**,**d**,**f**,**h**) as for n = 0.05, 0.10, 0.15, 0.20 (from top to bottom; simulations n-1, n-2, n-3, and n-4, respectively).

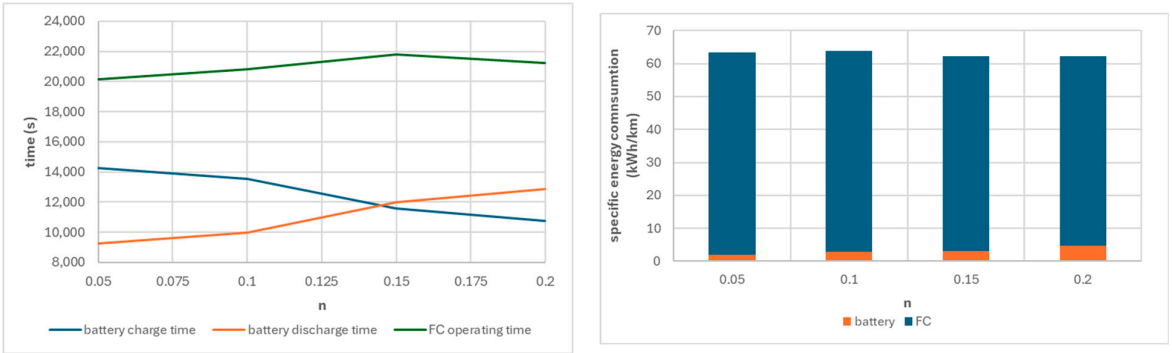


Figure 8. Operating time (**left**) and specific energy consumption (**right**) as a function of n.

The FC operating time also increases with n, but peaks at $n = 0.15$. In fact, in the case of $n = 0.10$, the battery has limited capacity and quickly reaches its minimum SOC. As a result, the fuel cell is frequently switched on to recharge the battery, but the limited recharge capacity and high-power demand prevents a stable increase in SOC. This leads to frequent transitions between ON and idle states, increasing the number of variable load cycles and degradation. Conversely, with $n = 0.15$, the battery discharges more slowly and is capable of regaining charge beyond the minimum SOC threshold thanks to longer charging phases. However, the SOC never reaches a value high enough to deactivate the recharge mode, and the EMS logic keeps the FC active to maintain SOC stability and assist in supplying power. As a result, the FC experiences fewer cycles at variable load but remains active longer overall. This explains the observed peak in fuel cell operating time at $n = 0.15$ despite lower degradation and replacements.

The influence of n on the specific energy consumption is illustrated in Figure 8-right. As n increases, the battery contribution grows significantly, from 1.99 kWh/km at $n = 0.05$ to 4.74 kWh/km at $n = 0.20$. In contrast, the energy consumption of the fuel cell decreases with increasing n, dropping from 61.32 kWh/km to 57.47 kWh/km over the same range. Nevertheless, the fuel cell remains the dominant contributor to the total specific energy consumption across all configurations.

The FC and battery degradations result in different replacement trends (Table 9). While the number of battery replacements decreases (though not linearly) as n increases, the number of FC replacements exhibits a peak at $n = 0.10$ before decreasing. As in the previous simulations (varying m), this trend reflects the variation in the number of load variation cycles experienced by the FC. Specifically, with lower n, the battery reaches its minimum SOC more frequently and struggles to recharge effectively, triggering frequent ON/OFF transitions in the FC. This intensifies degradation due to variable load operation. At $n = 0.15$, although the battery is larger and its SOC rises more effectively, the EMS logic keeps the FC active for longer periods to stabilize the SOC, resulting in longer continuous operation but fewer transitions—hence, reduced degradation. This explains the observed non-monotonic behavior in FC replacements.

Table 9. Summary of the degradation indicators and component replacements in 20 years for both the fuel cell (FC) and the battery, as a function of n.

FC Degradation Parameters	$n = 0.05$	$n = 0.10$	$n = 0.15$	$n = 0.20$
Idling time per hour (s/km)	3352	2717	1793	2375
Time of the high-power load operation (s)	20,153	20,832	21,794	21,250
Number of ON/OFF cycles per km	1	1	1	1
Number of cycles at variable load per km	219	394	190	178
# of FC replacements in 20 years	6	8	5	5
Battery degradation parameters	$n = 0.05$	$n = 0.10$	$n = 0.15$	$n = 0.20$
SOC_{min}	0.000	0.233	0.277	0.288
Equivalent cycles	8.84	4.64	3.35	2.30
Average DoD per cycle	0.986	0.960	0.973	0.073
# of battery replacements in 20 years	12	6	5	3

Regarding the battery, the Rainflow cycle counting analysis highlights that the equivalent number of full cycles consistently decreases with n, from 8.84 at $n = 0.05$ down to 2.30 at $n = 0.20$. This reduction reflects the lower cycling stress experienced by a larger battery. At the same time, the average depth of discharge (DoD) per cycle remains very high (>0.95) in all cases, indicating that the battery continues to operate under deep discharge conditions regardless of n. Consequently, although higher n values mitigate degradation by reducing

the number of equivalent cycles, the high DoD per cycle still accelerates aging, explaining why multiple replacements are required even in the most favorable case.

As in the previous analysis, the effectiveness of each configuration is assessed based on the total cost per kilometer. Figure 9 illustrates the variation in total cost as a function of n. The highest cost is observed at n = 0.10 (about 5.3 €/km), which corresponds to the maximum number of fuel cell replacements (eight) together with six battery replacements. Increasing n reduces the cycling stress on both components: at n = 0.15 and n = 0.20, the number of replacements decreases to five for the fuel cell and three for the battery, bringing the total cost down to about 4.5 €/km. The configuration with n = 0.05, although showing a slightly lower total cost than n = 0.10 (about 4.5 €/km), is not technically viable. As shown in Figure 6-b, the SOC frequently drops below the admissible minimum value and even reaches zero in several parts of the route, a condition that would prevent safe operation. The case with n = 0.10 is borderline: the SOC fluctuates around the minimum admissible level but never reaches zero, which means the route can be completed, albeit under critical operating conditions.

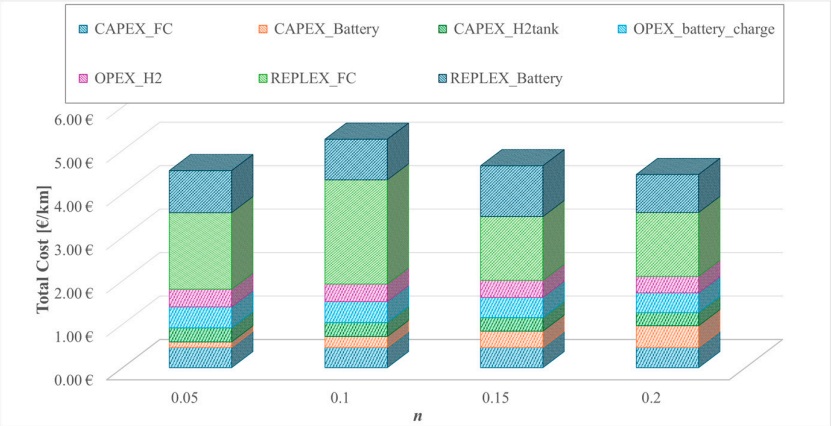


Figure 9. Breakdown of total costs as a function of n.

The cost breakdown in Figure 9 shows that, under the assumed energy prices, the dominant contributions are the replacement costs of the electrochemical components. At n = 0.10, the large number of FC and battery replacements strongly increases the total cost. As n increases, the reduction in replacement frequency clearly outweighs the higher investment cost of a larger battery (CAPEX_Battery), explaining the progressive decrease in total cost. These results underline that the optimal n is not only a matter of minimizing energy use but also of mitigating component aging, which has a stronger impact on the long-term economic performance of the system.

4.3. Effect of the Route

The effects of n and m on the behavior of the system were studied considering the SIL route. This route is a completely flat 177.5 km long rail track, but it is not representative of all possible routes. Thus, to study the effect of the route characteristics on the behavior of the system, three different tracks have been considered, namely SIL, CIL and NIL routes (Table 6). In this analysis, the fuel cell and battery sizing were kept constant with values m = 0.45 and of n = 0.20.

The behavior of the train running on different route is evident when looking at the power and SOC curves (Figure 10 left and right, respectively): the maximum requested power is about the same (as it depends on the motor maximum traction force which also was kept constant), but the answer of the powertrain (FC and battery power sharing) varies with the route. On the SIL track (Figure 10a,b) the power request is quite regular, with a

peak power at the start, followed by a steady state and then by a braking phase to the next stop. Since the power request is greater than the FC power, the battery is used to cover the gap. This results in a constant decrease in the battery SOC, with the braking phase as the only recharging source. As the minimum admitted SOC (0.3) is reached, then the FC helps the recharging phase, thus keeping the SOC always above its minimum. In the CIL route (Figure 10c,d), the situation is different: the stops are distributed less regularly along the track and climbs and descents are present. In the first part of the route, the behavior of the powertrain is similar to that in the SIL track, with the battery often acting to cover the gap between the power demand and the FC power. The battery SOC decreases to the minimum at about 1500 s and then stays at about 0.15 until 4300 s. Between 4300 s and 6200 s, a descent part in the route drastically reduces the power request, resulting in a great possibility for the FC to recharge the battery. This brings the battery SOC up to the starting value and allows the battery to operate above the minimum SOC until the end of the track. On the NIL route (Figure 10e,f), climbs and descents are distributed along the track, and the power request is less regular in comparison with that of the SIL and CIL routes. The battery SOC decreases below the minimum but then, the descents between some stops in the second half of the route helps the FC to recharge the battery, keeping the battery SOC above the minimum until the end.

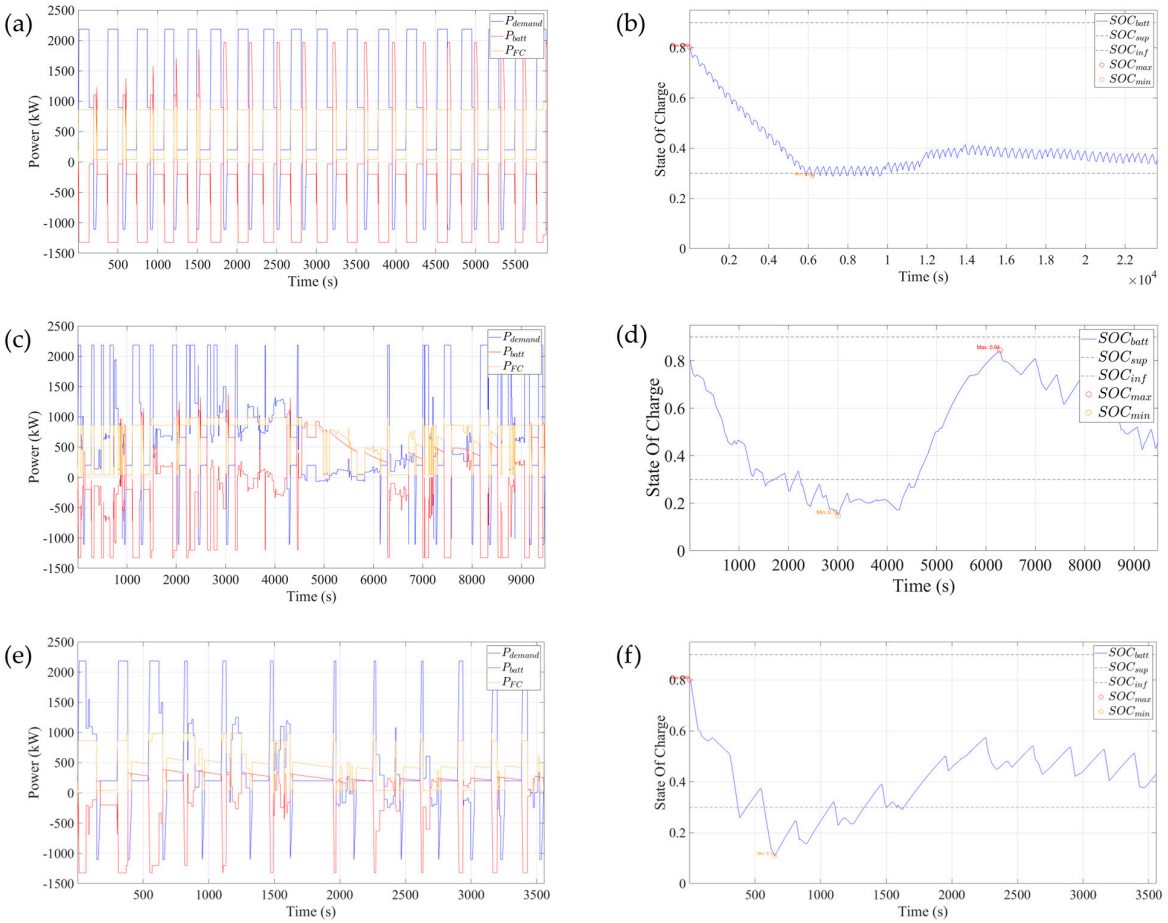


Figure 10. Power (**a**,**c**,**e**) and state of charge of the battery (**b**,**d**,**f**) in SIL, CIL and NIL routes (from top to bottom; simulations *route*-1, *route*-2, and *route*-3, respectively). Only in this analysis the power plot of the SIL route shows the whole extension of the track.

Figure 11 shows the battery and FC operating times (left) and the specific energy consumption (right) as a function of the route considered. Although it may appear counter-intuitive, the SIL route shows the highest specific energy consumption mainly because of

its higher operating speeds and station density. In fact, as evident from Table 6 SIL allows long cruising at 130 km/h, which amplifies aerodynamic drag and rolling resistance, and it presents 0.21 stations/km (37 stations over 177.5 km), more than twice the density of CIL (0.085 stations/km). This results in frequent accelerations from standstill, which are particularly energy-intensive. By contrast, in CIL and NIL the presence of gradients offers more opportunities for regenerative braking, reducing the net specific energy consumption. Since the routes have different characteristics, in this case the operating times have been normalized by the route length. Both charts in Figure 11 clearly indicate that the CIL route seems the one in which powertrain performance are optimal: the battery charge and discharge time, as well as the FC operating time, are the lowest, which results in the smallest energy consumption per km. However, besides the operating times, it is important to assess how the battery and the FC operates. Table 10 resumes the main parameters affecting the FC degradation, and the battery and FC number of replacements.

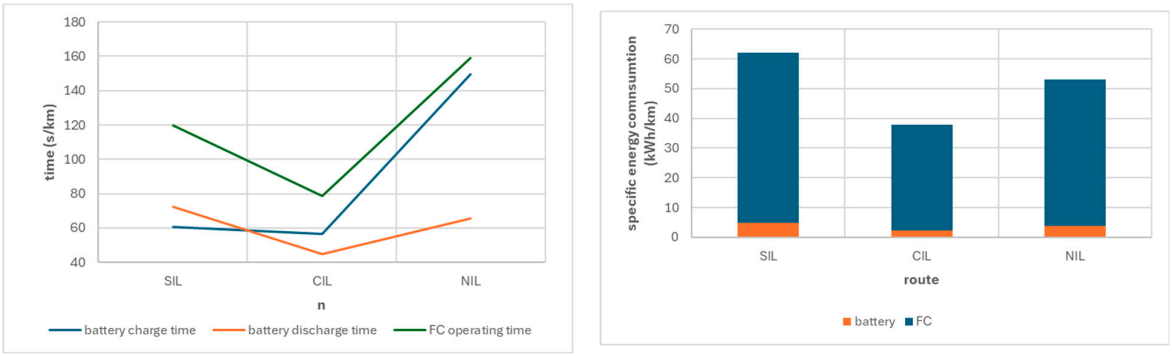


Figure 11. Operating time (**left**) and specific energy consumption (**right**) as a function of the route.

Table 10. Summary of the degradation indicators and component replacements in 20 years for both the fuel cell (FC) and the battery, as a function of the route.

FC Degradation Parameters	SIL	CIL	NIL
Idling time per hour (s/km)	2375	2120	932
Time of the high-power load operation (s)	119.7	35.7	5.1
Number of ON/OFF cycles per km	1	1	1
Number of cycles at variable load per km	1.0	11.5	10.3
# of FC replacements in 20 years	5	23	20
Battery degradation parameters	**SIL**	**CIL**	**NIL**
SOC_{min}	0.288	0.149	0.109
Equivalent cycles	2.50	1.81	1.67
Average DoD per cycle	0.973	0.900	0.900
# of battery replacements in 20 years	3	2	2

Focusing on the FC, the degradation behavior is strongly route-dependent. On the SIL route, the FC experiences long periods of continuous operation at high power but with relatively few load variation cycles (about 1 cycle/km). This operating profile results in only five replacements over 20 years, showing that stable operation, even at higher energy demand, is less detrimental than frequent transients. By contrast, the CIL and NIL routes, characterized by frequent gradients and irregular stop distribution, lead to a high number of variable load cycles (about 10–12 cycles/km). These conditions cause repeated load fluctuations, which are particularly harmful for FC durability, leading to 23 replacements for the CIL route and 20 for the NIL route. This confirms that FC aging is primarily accelerated by transient operation rather than by sustained high-power use.

Concerning the battery, the Rainflow analysis shows that the equivalent number of full cycles remains modest across all routes, ranging from 1.67 (NIL) to 2.50 (SIL) over the 20-year horizon. This explains why the number of battery replacements is limited to 2–3 in all cases. At the same time, the average depth of discharge per cycle stays very high (about 0.90–0.97), indicating that the battery continues to undergo deep cycling regardless of the route. In particular, the SIL route, being longer and with higher continuous power demand, results in the highest equivalent cycles (2.50) and thus the largest number of replacements (three), while the NIL route—shorter and less demanding—exhibits the lowest cycle count (1.67) and only two replacements. These results suggest that, unlike the FC whose aging is strongly affected by route-specific cycling patterns, the battery degradation is primarily driven by the consistently high DoD, with route length and load profile influencing the replacement count only marginally.

Figure 12 reports the breakdown of total costs (€/km) for the three analyzed routes, considering the same hybrid powertrain sizing (m = 0.45, n = 0.20). Interestingly, despite the CIL and NIL routes showing the lowest specific energy consumption (Figure 11-right), their total cost per kilometer is significantly higher than that of the SIL route. This counter-intuitive result is primarily driven by the different degradation behaviors of the fuel cell, which strongly depend on the route characteristics. The intensive fuel cell degradation in CIL and NIL routes effects result in REPLEX_FC costs of 13.40 €/km (CIL) and 67.10 €/km (NIL), which are the main contributors to the high total costs of 15.80 €/km and 76.69 €/km, respectively. By contrast, the SIL route, despite being the most energy-demanding, allows for a more stable and continuous FC operation resulting in only 5 FC replacements and 3 battery replacements over the simulation horizon, corresponding to total costs of 4.44 €/km, the lowest among all cases. The cost breakdown clearly shows that degradation-induced REPLEX are the dominant contributors to the economic sustainability of the system, far more impactful than the operational costs (OPEX_H2 and OPEX_battery_charge), which remain below 0.5 €/km in all cases. Even the CAPEX are comparable across routes and represent only a minor share of the total cost. This confirms that route-induced FC degradation is the key driver of long-term cost differences and must be explicitly considered in the sizing and control strategy of hybrid trains. Ultimately, these results suggest that a one-size-fits-all configuration is not viable: although m = 0.45 and n = 0.20 work well for the SIL route, they are clearly unsuitable for shorter or more irregular profiles like NIL and CIL. Route-specific sizing and EMS tuning are therefore essential to minimize degradation and ensure economic viability.

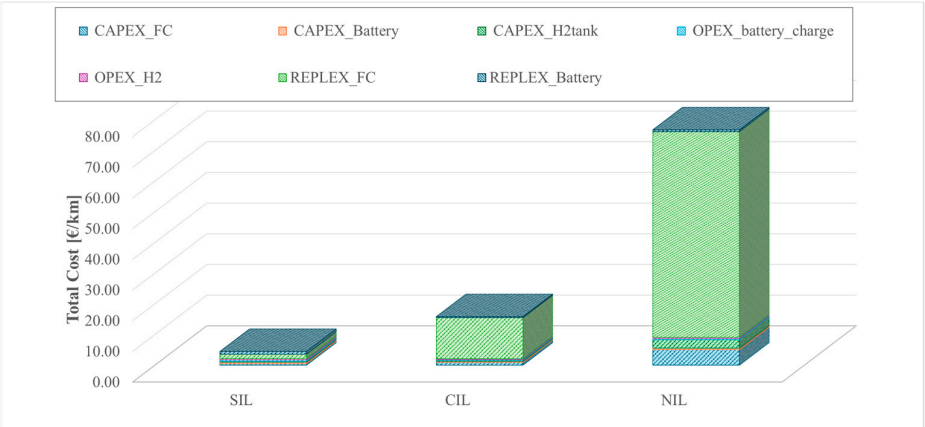


Figure 12. Breakdown of total costs as a function of the route.

5. Conclusions

In this work, a complete numerical model has been developed in MATLAB to simulate the dynamic behavior of a hybrid fuel cell–battery train. The proposed tool is highly flexible and can be adapted to simulate any train configuration, route, and control strategy, provided that the input data regarding the route and train characteristics are available. The model enables both detailed energy analyses—tracking power flows, battery SOC, and component-specific consumption—and long-term techno-economic assessments over a user-defined time horizon. This dual perspective allows for evaluating efficiency, degradation, and lifecycle cost in an integrated manner.

In the present study, we focused on a sensitivity analysis of the two most influential sizing parameters: the nominal power of the fuel cell (parameter m) and the total capacity of the battery pack (parameter n). Furthermore, we analyzed the performance of one of the hybrid configurations across different real-world railway routes. The control logic adopted here is a rule-based EMS, designed to minimize hydrogen consumption and reduce fuel cell degradation, which are the most economically influent factors over the vehicle lifetime.

Key findings of the sensitivity analysis are summarized below:

- Fuel cell power ratio (m): Increasing m improves energy efficiency, since FC consumption decreases and the battery SOC is more easily stabilized, but it also accelerates component degradation. At m = 0.40, the total cost is lowest (about 4.0 €/km) with only five FC and six battery replacements, but this configuration is not technically viable on the SIL route because the SOC drops below the admissible threshold. At m = 0.45, costs peak at about 5.1 €/km due to eight FC replacements, while at m = 0.50 replacements slightly improve (seven FC and seven batteries) with a nearly unchanged cost (about 5.1 €/km). Overall, m = 0.50 represents a marginally better compromise than m = 0.45.
- Battery capacity ratio (n): Increasing n enhances the contribution of the battery to traction, reduces the frequency of critical SOC events, and lowers the cycling stress on both components. However, the effect on the fuel cell is non-monotonic: at n = 0.10 the battery is too small, forcing frequent FC ON/OFF transitions and leading to eight FC replacements and six battery replacements, with the highest lifecycle cost (about 5.3 €/km). Increasing to n = 0.15–0.20 stabilizes SOC and reduces replacements (five FC and three batteries), bringing the cost down to about 4.5 €/km (–15% compared to n = 0.10). The case with n = 0.05 shows a similar cost (about 4.5 €/km) but is not technically viable, since SOC often falls below the admissible minimum. Overall, the results underline that the economic optimum is not only driven by minimizing energy use but rather by mitigating degradation, with replacement costs remaining the dominant factor.
- Route sensitivity: The analysis shows that fuel cell degradation is strongly dependent on the operational profile. On the SIL route, characterized by regular load and continuous high-power operation, the FC undergoes only five replacements in 20 years and the total cost is the lowest (about 4.44 €/km). By contrast, on CIL and NIL, frequent gradients and irregular stop distributions cause 23 and 20 FC replacements, respectively in the 20 years time horizon here considered. This drastically increases costs to 15.8 €/km on CIL (+255% vs. SIL) and 76.7 €/km on NIL (+1600% vs. SIL). Although CIL and NIL exhibit lower specific energy consumption thanks to regenerative braking, this advantage is overwhelmed by the accelerated FC degradation. Battery replacements remain limited (2–3 over 20 years) and show only minor route dependence. Overall, these results confirm that a one-size-fits-all sizing strategy is not viable. For shorter routes such as CIL and NIL, a possible way to reduce the number of FC replacements is to reduce cycling stress by increasing n (larger battery capacity)

and decreasing m (lower FC share of nominal power). In this configuration, the FC operates under steadier conditions while the battery buffers short-term fluctuations, mitigating stack degradation. Conversely, preliminary optimization results indicate that for longer routes a higher m is required to guarantee sufficient onboard energy.

Despite the robustness of the framework, some limitations must be acknowledged. Component degradation was modeled through simplified empirical rules, while hydrogen and electricity prices were assumed constant. Moreover, the EMS was kept rule-based and not optimized. These simplifications may affect quantitative results, although the relative trends remain meaningful. Future work will integrate more detailed electrochemical models, dynamic cost scenarios, and optimized EMS strategies.

Overall, the study demonstrates that hybrid train sizing cannot rely on generic configurations: powertrain parameters must be optimized not only for energy efficiency but also for long-term economic sustainability, with explicit consideration of route-specific features. This highlights the need for a paradigm shift from "all-purpose" trains toward specialized, context-adapted solutions. As a next step, a detailed route-specific optimization process should be carried out, since the train energy behavior and degradation trends vary considerably depending on the operational context.

Author Contributions: Conceptualization, G.A. and P.V.; Methodology, G.A., A.R. and P.V.; Software, G.A., A.R. and P.V.; Validation, A.R. and P.V.; Formal analysis, A.R.; Investigation, G.A. and P.V.; Data curation, G.A. and P.V.; Writing—original draft, G.A. and A.R.; Writing—review & editing, D.B. and P.V.; Supervision, D.B.; Project administration, D.B.; Funding acquisition, D.B. All authors have read and agreed to the published version of the manuscript.

Funding: This research has been Funded by the Ministry of University and Research (MUR) as part of the European Union program NextGenerationEU, under the National Recovery and Resilience Plan (NRRP)—Sustainable mobility center, Spoke 4: Rail Transportation.

Data Availability Statement: The original contributions presented in this study are included in the article. Further inquiries can be directed to the corresponding author.

Conflicts of Interest: The authors declare no conflict of interest.

Nomenclature

Acronyms	
AGE	Total aging function of the battery
AGE_{cal}	Calendar aging of the battery
AGE_{cyc}	Cyclic aging of the battery
$\mathrm{AGE}(\Delta t)$	Aging over time interval Δt of the battery
a	Davis coefficient (N/t)
$a_{comfort}$	Comfort acceleration (m/s^2)
b	Davis coefficient (N/(t·km/h))
C-rate	Charge/discharge rate of the battery
CAPEX	Capital Expenditure
CIL	Center Italy Line
C_{string}	Capacity of a battery string (kWh)
C_{tot}	Total battery capacity (kWh)
c	Davis coefficient (N/(t·(km/h)^2))
DoD	Degree of discharge of the battery
d	Technology specific constant for the battery degradation model
$dec_{comfort}$	Comfort deceleration (m/s^2)
$dist_{trip}$	Round trip distance (km)
E_{batt}	Battery capacity (kWh)
E_{cyc}	Energy exchanged per cycle by the battery (kWh)

$E_{tot,batt}$	Energy that is supposed to be covered by battery (kWh)
$\overline{E_{id}}$ about 1.17	Theoretical FC open-circuit potential (V)
EMS	Energy Management System
$F = 96485\ \mathrm{C/mol}$	Faraday constant
FC	Fuel Cell
FCV	Fuel Cell Vehicle
f	Generic function
$f_{conv} = 0.0224136\ \left(\mathrm{Nm^3/mol}\right)$	Conversion factor
f_0	Static adhesion coefficient
g	Gravity acceleration ($\mathrm{m/s^2}$)
HIL	Hardware-in-the-Loop
$H_{2,\mathrm{requested}}$	Hydrogen required by the fuel cell (kg)
I	Inertial force (kN)
I_{batt}	Battery current (A)
I_{dens}	Actual current density ($\mathrm{A/cm^2}$)
$I_{\mathrm{dens},0}$	Reference current density ($\mathrm{A/cm^2}$)
I_{FC}	FC current (A)
I_{OC}	Open-circuit current (A)
I_{string}	String current (A)
i	Slope (‰)
j	Technology specific constant for the battery degradation model
$k = 1.72$	Calibration factor of the FC derating model
k_s	Empirical coefficient (Ohm)
$LHV_{H2} = 120\ \mathrm{MJ/kg}$	H_2 lower heating value
$MW_{\mathrm{H_2}}$	Molar mass of H_2 (kg/kmol)
m_e	Equivalent mass (t)
m_v	Vehicle mass (t)
$\dot{m}_{\mathrm{H_2}}$	Hydrogen consumption (kg/s)
m_0	Adhesion ratio
N_{cyc}	Number of cycles of the battery
NIL	North Italy Line
NL	Normalize H_2 storage level (-)
$n_{\mathrm{batt,cell}}$	Number of cells in a battery
n_{cells}	Number of cells in the FC
n_{stack}	Number of parallel stacks in the FC
n_{string}	Number of parallel strings in the battery
$n_{trips,year}$	Number of journeys per year
n_1	Average start–stop cycles per hour (-/h)
n_2	Average cycles during the load change phase (-/h)
OCV	Open-circuit voltage
P	Power required to vehicle motion (kW)
P_{aux}	Auxiliary power request (kW)
P_{batt}	Power provided by the battery (kW)
$P_{ch/dis}$	Charge/discharge power of the battery (kW)
P_{demand}	Power request by the electric motor (kW)
P_{FC}	FC power (kW)
$P_{idling,FC}$	FC idling power (kW)
$P_{lower,FC}$	Lower operational FC power (kW)
$P_{max,FC}$	FC maximum power (kW)
P_{mech}	Power request at the electric motor shaft (kW)
$P_{nom,FC}$	FC nominal power (kW)
$P_{upper,FC}$	Upper operational FC power (kW)
p_{in}	Initial pressure (Pa)
p_{fin}	Final pressure (Pa)

$p_{\max}$	Maximum pressure of the H_2 storage tank (Pa)
$R = 8.314 J/(mol \cdot K)$	Universal gas constant
$R_{bat,tot}$	Total equivalent resistance of the battery (Ohm)
R_{gra}	Grade resistance (kN)
R_{ohm}	Resistance of the battery (Ohm)
R_{ord}	Ordinary resistance to motion (kN)
R_{string}	Internal resistance of a string (Ohm)
R_{tot}	Total resistance to motion (kN)
R_{wire}	Wire resistance of the cables associated with a string (Ohm)
SIL	South Italy Line
SOC	State of charge (-)
SOC_{string}	Current state of charge of a string (-)
$SOC_{string,0}$	Initial state of charge of a string (-)
SoH	State of health of the battery
SoH_{end}	State of health of the battery at the end of a time step
SoH_{start}	Initial state of health of the battery
sc	Specific cost (€/km)
T	Temperature (K)
$T(v)$	Traction force at a given train speed (kN)
T_{batt}	Battery operating temperature (K)
T_{life}	Nominal lifetime of the battery (h)
t	Time (s)
t_{FC}	FC lifetime (h)
t_1	Average idling time per hour (h)
t_2	Average time of the high-power load operation (h)
U_1	Voltage degradation due to idling (μV/h)
U_2	Voltage degradation due to high-power operation (μV/h)
V_{batt}	Battery voltage (V)
$V_{batt,cell}$	Single battery cell voltage (V)
V_{FC}	FC voltage (V)
V_{cell}	Cell voltage (V)
V_{deg}	Voltage decay rate (V/h)
$V_{OC,i}$	Open circuit voltage of the i-th string of the battery (V)
V_1	Voltage degradation due to start–stop cycles (μV/cycle)
V_2	Voltage degradation due to load-change cycles (μV/cycle)
$vol_{storage}$	H_2 storage volume (m^3)
ΔSoH	Variation in the state of health of the battery
ΔV	Voltage derating of the FC per route (V/route)
ΔV_{act}	Activation loss (V)
ΔV_{conc}	Concentration loss (V)
ΔV_{ohm}	Ohmic loss (V)
Δp	Pressure variation (Pa)
Δt	Time interval (s)
Δvol	Volume variation in the H_2 storage tank (m3)
v	Train speed (km/h)
$z = 2$	Number of electrons transferred per H_2 molecule
Greek letters	
β	Mass augmentation coefficient for rotating or translating masses (-)
η_{FC}	Efficiency of the FC (-)
η_{mot}	Efficiency of the electric motor (-)
η_{inv}	Efficiency of the DC-AC inverter (-)
η_{convr}	Efficiency of the DC-DC converter (-)
η_t	Transmission efficiency (-)
ρ_{H2}	H_2 density (kg/m^3)

References

1. Report from the Commission to the European Parliament and the Council-Eighth Monitoring Report on the Development of the Rail Market Under Article 15(4) of Directive 2012/34/EU of the European Parliament and of the Council, European Commission, COM(2023) 510 final, Brussels, 13.9.2023. Available online: https://eur-lex.europa.eu/legal-content/EN/TXT/?uri=CELEX%3A52023DC0510 (accessed on 1 October 2025).
2. Transport & Environment. *Emission Reduction Strategies for the Transport Sector in Italy*; European Federation for Transport and Environment (T&E): Brussels, Belgium, 2019.
3. Gad, K.S.; Tonini, F.; Agati, G.; Borello, D.; Colombo, E. Energy demand prediction and scenario analysis for vehicle traction: A bottom-up approach applied to the Italian railway system. *Energy Rep.* **2025**, *13*, 4196–4208. [CrossRef]
4. Fuel Cells and Hydrogen Joint Undertaking. Hydrogen Roadmap Europe: A sustainable pathway for the European Energy Transition. *Publications Office.* 2019. Available online: https://data.europa.eu/doi/10.2843/341510 (accessed on 1 October 2025).
5. Staffell, I.; Scamman, D.; Abad, A.V.; Balcombe, P.; Dodds, P.; Ekins, P.; Shah, N.; Ward, K. The role of hydrogen and fuel cells in the global energy system. *Energy Environ. Sci.* **2018**, *12*, 463–491. [CrossRef]
6. Pagand, I. *Fostering the Railway Sector Through the European Green Deal*; European Union Agency for Railways: Valenciennes, France, 2020.
7. Agati, G.; Borello, D.; Migliarese Caputi, M.V.; Cedola, L.; Gagliardi, G.G.; Pozzessere, A.; Venturini, P. Effect of the Degree of Hybridization and Energy Management Strategy on the Performance of a Fuel Cell/Battery Vehicle in Real-World Driving Cycles. *Energies* **2024**, *17*, 729. [CrossRef]
8. Fragiacomo, P.; Piraino, F.; Genovese, M.; Flaccomio Nardi Dei, L.; Donati, D.; Migliarese Caputi, M.V.; Borello, D. Sizing and performance analysis of hydrogen- and battery-based powertrains, integrated into a passenger train for a regional track, located in Calabria (Italy). *Energies* **2022**, *15*, 6004. [CrossRef]
9. Tao, S.; Chen, W.; Gan, R.; Li, L.; Zhang, G.; Han, Y.; Li, Q. Energy management strategy based on dynamic programming with durability extension for fuel cell hybrid tramway. *Railw. Eng. Sci.* **2021**, *29*, 299–313. [CrossRef]
10. Al-Hamed, K.H.M.; Dincer, I. A novel ammonia molten alkaline fuel cell based integrated powering system for clean rail transportation. *Energy* **2020**, *201*, 117620. [CrossRef]
11. Sorrentino, M.; Agbli, K.S.; Hissel, D.; Chauvet, F.; Letrouve, T. Application of dynamic programming to optimal energy management of grid-independent hybrid railcars. *Proc. Inst. Mech. Eng. Part F J. Rail Rapid Transit* **2021**, *235*, 236–247.
12. Jung, J.; Kim, D.; Yang, L.; Kim, N. Optimal energy management strategy for repeat path operating fuel cell hybrid tram. *Energies* **2024**, *17*, 1560. [CrossRef]
13. Yang, J.; Xu, X.; Peng, Y.; Zhang, J.; Song, P. Modeling and optimal energy management strategy for a catenarybattery-ultracapacitor based hybrid tramway. *Energy* **2019**, *183*, 1123–1135.
14. Yang, J.; Xu, X.; Peng, Y.; Deng, P.; Wu, X.; Zhang, J. Hierarchical energy management of a hybrid propulsion system considering speed profile optimization. *Energy* **2022**, *244*, 123098. [CrossRef]
15. Song, K.; Huang, X.; Xu, H.; Sunc, H.; Chen, Y.; Huang, D. Model predictive control energy management strategy integrating long short-term memory and dynamic programming for fuel cell vehicles. *Int. J. Hydrogen Energy* **2024**, *56*, 1235–1248. [CrossRef]
16. Vieira, G.T.T.; Furquim Pereira, D.; Iman Taheri, S.; Khan, K.S.; Salles, M.B.C.; Guerrero, J.M.; Carmo, B.S. Optimized configuration of diesel engine-fuel cell-battery hybrid power systems in a platform supply vessel to reduce CO_2 emissions. *Energies* **2022**, *15*, 2184. [CrossRef]
17. Nikiforow, K.; Pennanen, J.; Ihonen, J.; Uski, S.; Koski, P. Power ramp rate capabilities of a 5 kW proton exchange membrane fuel cell system with discrete ejector control. *J. Power Sources* **2018**, *381*, 30–37. [CrossRef]
18. Chen, H.; Jia, S.; Liu, B.; Zhang, T. Numerical Simulation of the Power Performance a Proton Exchange Membrane Fuel Cell Under Dynamic Loading Conditions. *IEEE Access* **2018**, *6*, 67992–68000. [CrossRef]
19. Edwards, R.L.; Demuren, A. Regression analysis of PEM fuel cell transient response. *Int. J. Energy Environ. Eng.* **2016**, *7*, 329–341. [CrossRef]
20. San Martín, I.; Ursúa, A.; Sanchis, P. Modelling of PEM Fuel Cell Performance: Steady-State and Dynamic Experimental Validation. *Energies* **2014**, *7*, 670–700. [CrossRef]
21. Liu, X.; Li, K. Energy Storage Devices in Electrified Railway Systems: A Review. *Transp. Saf. Environ.* **2020**, *2*, 183–201. [CrossRef]
22. Goolak, S.; Kondratieva, L.; Riabov, I.; Lukoševičius, V.; Keršys, A.; Makaras, R. Research and Optimization of Hybrid On-Board Energy Storage System of an Electric Locomotive for Quarry Rail Transport. *Energies* **2023**, *16*, 3293. [CrossRef]
23. Royston, S.J.; Gladwin, D.T.; Stone, D.A.; Ollerenshaw, R.; Clark, P. Development and Validation of a Battery Model for Battery Electric Multiple Unit Trains. In Proceedings of the IECON 2019—45th Annual Conference of the IEEE Industrial Electronics Society, Lisbon, Portugal, 14–17 October 2019; pp. 4563–4568. [CrossRef]
24. Ruvio, A.; Bayrak, O. A preliminary design of a hybrid train's on-board batteries for a 25 kV- 50 Hz high speed railway line. *J. Energy Storage* **2024**, *84 Pt B*, 110966. [CrossRef]

25. Alstom. World Premiere: Alstom's Hydrogen Trains Enter Passenger Service in Lower Saxony. 2018. Available online: https://www.alstom.com/press-releases-news/2018/9/world-premiere-alstoms-hydrogen-trains-enter-passenger-service-lower (accessed on 1 April 2025).
26. Gallucci, M. Hydrogen trains roll into service: A new hybrid locomotive signals a growing push for zero-emission rail technologies. *IEEE Spectr.* **2019**, *56*, 6–7. [CrossRef]
27. Alstom. Alstom's Coradia iLint Hydrogen Train Runs for the First Time in France. Available online: https://www.alstom.com/press-releases-news/2021/9/alstoms-coradia-ilint-hydrogen-train-runs-first-time-france (accessed on 1 April 2025).
28. Refuelling and Safety Tests Begin for Italy's First Hydrogen Train. Available online: www.rinnovabili.it (accessed on 1 February 2024). (In Italian).
29. European Environment Agency. Available online: www.eea.europa.eu (accessed on 1 April 2025).
30. Fedele, E.; Iannuzzi, D.; Del Pizzo, A. Onboard energy storage in rail transport: Review of real applications and techno--economic assessments. *IET Electr. Syst. Transp.* **2021**, *11*, 279–309. [CrossRef]
31. Materials and Drives for High & Widec Efficiency Electric Powertrains–Final Report. Hi-Wi, FP7 Project ID 266084. Available online: https://cordis.europa.eu/project/id/266084/reporting (accessed on 1 April 2025).
32. Arsene, S.; Sebesan, I. Analyze of aerodynamic forces acting on the Siemens Desiro railcar. *Incas Bull.* **2016**, *8*, 15.
33. Lamedica, R.; Ruvio, A.; Tobia, M.; Buffarini, G.G.; Carones, N. A preliminary techno-economic comparison between DC electrification and trains with on-board energy storage systems. *Energies* **2020**, *13*, 6702. [CrossRef]
34. Akroot, A.; Ekici, Ö.; Köksal, M. Process modeling of an automotive pem fuel cell system. *Int. J. Green Energy* **2019**, *16*, 778–788. [CrossRef]
35. MathWorks, Battery Equivalent Circuit–Simscape Battery. Available online: https://it.mathworks.com/help/simscape-battery/ref/batteryequivalentcircuit.html (accessed on 1 September 2025).
36. Zhao, N.; Chu, Y.; Xie, Z.; Eggen, K.; Girard, F.; Shi, Z. Effects of Fuel Cell Operating Conditions on Proton Exchange Membrane Durability at Open-Circuit Voltage. *Fuel Cells* **2020**, *20*, 176–184. [CrossRef]
37. Bai, X.; Luo, L.; Huang, B.; Jian, Q.; Cheng, Z. Performance improvement of proton exchange membrane fuel cell stack by dual-path hydrogen supply. *Energy* **2022**, *246*, 123297. [CrossRef]
38. Nguyen, H.L.; Han, J.; Nguyen, X.L.; Yu, S.; Goo, Y.-M.; Le, D.D. Review of the Durability of Polymer Electrolyte Membrane Fuel Cell in Long-Term Operation: Main Influencing Parameters and Testing Protocols. *Energies* **2021**, *14*, 4048. [CrossRef]
39. Zhao, Y.; Li, X.; Li, W.; Wang, Z.; Wang, S.; Xie, X.; Ramani, V. A high-performance membrane electrode assembly for polymer electrolyte membrane fuel cell with poly(arylene ether sulfone) nanofibers as effective membrane reinforcements. *J. Power Sources* **2019**, *444*, 227250. [CrossRef]
40. Pivac, I.; Bezmalinović, D.; Barbir, F. Catalyst degradation diagnostics of proton exchange membrane fuel cells using electrochemical impedance spectroscopy. *Int. J. Hydrogen Energy* **2018**, *43*, 13512–13520. [CrossRef]
41. Zhao, Y.; Wang, Q.; Xu, L.; Hu, Z.; Jia, X.; Qin, Z.; Li, J.; Ouyang, M. Characteristic Analysis of Fuel Cell Decay Based on Actual Vehicle Operating Conditions. In Proceedings of the IEEE 4th International Electrical and Energy Conference (CIEEC), Wuhan, China, 28–30 May 2021.
42. Chen, H.; Pei, P.; Song, M. Lifetime prediction and the economic lifetime of Proton Exchange Membrane fuel cells. *Appl. Energy* **2015**, *142*, 154–163. [CrossRef]
43. Omar, N.; Monem, M.A.; Firouz, Y.; Salminen, J.; Smekens, J.; Hegazy, O.; Gaulous, H.; Mulder, G.; Van Den Bossche, P.; Coosemans, T.; et al. Lithium iron phosphate based battery—Assessment of the aging parameters and development of cycle life model. *Appl. Energy* **2014**, *113*, 1575–1585. [CrossRef]
44. Saw, L.H.; Somasundaram, K.; Ye, Y.; Tay, A.A.O. Electro-thermal analysis of Lithium Iron Phosphate battery for electric vehicles. *J. Power Sources* **2014**, *249*, 231–238. [CrossRef]
45. Kim, S.H.; Shin, Y.-J. Optimize the operating range for improving the cycle life of battery energy storage systems under uncertainty by managing the depth of discharge. *J. Energy Storage* **2023**, *73*, 109144. [CrossRef]
46. Torabi, F.; Ahmadi, P. Fundamentals of Batteries. In *Simulation of Battery Systems*; Elsevier: Amsterdam, The Netherlands, 2020; pp. 55–81. [CrossRef]
47. Masaud, T.M.; El-Saadany, E.F. Correlating Optimal Size, Cycle Life Estimation, and Technology Selection of Batteries: A Two-Stage Approach for Microgrid Applications. *IEEE Trans. Sustain. Energy* **2020**, *11*, 1257–1267. [CrossRef]
48. Wu, Y.; Liu, Z.; Liu, J.; Xiao, H.; Liu, R.; Zhang, L. Optimal battery capacity of grid-connected PV-battery systems considering battery degradation. *Renew. Energy* **2022**, *181*, 10–23. [CrossRef]
49. Magel, E.E. *A Survey of Wheel/Rail Friction*; U.S. Department of Transportation: Washington, DC, USA, 2017; DOT/FRA/ORD-17/21.
50. Kleen, G.; Gibbons, W. Heavy-Duty Fuel Cell System Cost–2023. In *DOE Hydrogen Program Record 24004*; United States Department of Energy: Washington, DC, USA, 2024.

51. BloombergNEF. Lithium-Ion Battery Pack Prices See Largest Drop Since 2017, Falling to $115 per Kilowatt-Hour. BloombergNEF, 2024/09/10. Available online: https://about.bnef.com/insights/commodities/lithium-ion-battery-pack-prices-see-largest-drop-since-2017-falling-to-115-per-kilowatt-hour-bloombergnef/ (accessed on 1 September 2025).
52. Houchins, C.; Prosser, J.H.; Graham, M.; Watts, Z.; James, B.D. Hydrogen Storage Cost Analysis: Project ST235, DOE Hydrogen Program. In Proceedings of the 2023 Annual Merit Review & Peer Evaluation Meeting, Arlington, VA, USA, 5–8 June 2023.
53. Eurostat, Electricity Price Statistics, Statistics Explained, European Commission. 2025. Available online: https://ec.europa.eu/eurostat/statistics-explained/index.php?title=Electricity_price_statistics (accessed on 1 September 2025).
54. Hubert, M.; Peterson, D.; Miller, E.; Vickers, J.; Mow, R.; Howe, C. Clean Hydrogen Production Cost Scenarios with PEM Electrolyzer Technology, DOE Hydrogen Program Record 24005. 2024. Available online: https://www.hydrogen.energy.gov/docs/hydrogenprogramlibraries/pdfs/24005-clean-hydrogen-production-cost-pem-electrolyzer.pdf (accessed on 1 September 2025).
55. Pugi, L.; Berzi, L.; Spedicato, M.; Cirillo, F. Hydrogen for railways: Design and simulation of an industrial benchmark study. *Int. J. Model. Identif. Control.* **2023**, *43*, 43–53. [CrossRef]
56. Pugi, L.; Berzi, L.; Cirillo, F.; Vecchi, A.; Pagliazzi, V. A tool for rapid simulation and sizing of hybrid traction systems with fuel cells. *Proc. Inst. Mech. Eng. Part F J. Rail Rapid Transit* **2023**, *237*, 104–113. [CrossRef]
57. Fioriti, D.; Scarpelli, C.; Pellegrino, L.; Lutzemberger, G.; Micolano, E.; Salamone, S. Battery lifetime of electric vehicles by novel rainflow-counting algorithm with temperature and C-rate dynamics: Effects of fast charging, user habits, vehicle-to-grid and climate zones. *J. Energy Storage* **2023**, *59*, 106458. [CrossRef]

Disclaimer/Publisher's Note: The statements, opinions and data contained in all publications are solely those of the individual author(s) and contributor(s) and not of MDPI and/or the editor(s). MDPI and/or the editor(s) disclaim responsibility for any injury to people or property resulting from any ideas, methods, instructions or products referred to in the content.